

AD-A232 935



AFOSR-TR- 01 0114
①

Annual Technical Report
for
AFOSR Grant No. 89-0185

FUNDAMENTAL STUDIES OF THE MECHANICAL BEHAVIOR OF MICROELECTRONIC
THIN FILM MATERIALS

Submitted to :

Department of the Air Force
Directorate of Electronic and Materials Sciences
Air Force Office of Scientific Research
Bolling Air Force Base, Building 410
Washington D.C. 20332

Attention: Dr. Gerald Witt

Submitted by:

Professor William D. Nix, Principal Investigator
Department of Materials Science and Engineering
Stanford University, Stanford, CA 94305

January 1991

DTIC
ELECTED
MAR 11 1991
S D

REPORT DOCUMENTATION PAGE

Form Approved
OMB No. 0704-0188

Public reporting burden for the collection of information is estimated to average 1 hour per response, including the time for reviewing instructions, searching existing data sources, gathering and maintaining the data needed, and completing and reviewing the collection of information. Send comments regarding this burden estimate or any other aspect of this collection of information, including suggestions for reducing this burden, to Washington Headquarters Services, Directorate for Information Operations and Analysis, 1215 Jefferson Davis Highway, Suite 1204, Arlington, VA 22202-4302, and to the Office of Management and Budget, Paperwork Reduction Project (0704-0188), Washington, DC 20503.

1. AGENCY USE ONLY (Leave blank)			2. REPORT DATE January 1, 1991		3. REPORT TYPE AND DATES COVERED Annual Report 11/15/89- 11/14/90	
4. TITLE AND SUBTITLE Fundamental Studies of the Mechanical Behavior of Microelectronic Thin Film Materials			5. FUNDING NUMBERS AFOSR Grant No. 89-0185			
6. AUTHOR(S) William D. Nix						
7. PERFORMING ORGANIZATION NAME(S) AND ADDRESS(ES) Department of Materials Science and Engineering Stanford University Stanford, CA 94305			8. PERFORMING ORGANIZATION REPORT NUMBER AFOSR- 91-1			
9. SPONSORING/MONITORING AGENCY NAME(S) AND ADDRESS(ES) Department of The Air Force Directorate of Electronic and Materials Sciences Air Force Office of Scientific Research Bolling AFB Washington D.C. 20332			10. SPONSORING/MONITORING AGENCY REPORT NUMBER 2305/C1			
11. SUPPLEMENTARY NOTES Attn: Dr. Gerald Witt						
12a. DISTRIBUTION/AVAILABILITY STATEMENT Unlimited				12b. DISTRIBUTION CODE		
13. ABSTRACT (Maximum 200 words) Research progress on the study of stresses and mechanical behavior of microelectronic thin films is reported. Specialized instruments have been developed to study stress relaxation in metal and semiconductor thin films, diffusion of water in passivation films and crystallization of amorphous silicon films. Finite element techniques have been used to determine stresses in passivated interconnect metal lines. These stresses have been used in a model of interconnect metal cracking that has been developed. It has been shown that the high concentrations of oxygen present in LRP Si-Ge films greatly inhibits misfit dislocation formation.						
14. SUBJECT TERMS Mechanical Properties of Thin Films, Stresses in Thin Films				15. NUMBER OF PAGES 70		
				16. PRICE CODE		
17. SECURITY CLASSIFICATION OF REPORT unclassified	18. SECURITY CLASSIFICATION OF THIS PAGE unclassified	19. SECURITY CLASSIFICATION OF ABSTRACT unclassified	20. LIMITATION OF ABSTRACT UL			

Annual Technical Report
for
AFOSR Grant No. 89-0185

FUNDAMENTAL STUDIES OF THE MECHANICAL BEHAVIOR OF MICROELECTRONIC
THIN FILM MATERIALS

Submitted to :

Department of the Air Force
Directorate of Electronic and Materials Sciences
Air Force Office of Scientific Research
Bolling Air Force Base, Building 410
Washington D.C. 20332

Attention: Dr. Gerald Witt

Submitted by:

Professor William D. Nix, Principal Investigator
Department of Materials Science and Engineering
Stanford University, Stanford, CA 94305

January 1991

Accession For	
NTIS	CRAsI
DTIC	TAB
Unannounced	
Justification	
By _____	
Distribution /	
Availability Copies	
Dist	Aval. at or Special
A-1	



This research was supported by the Air Force of Scientific Research (AFOSC) under Grant No. AFOSR-89-0185. Approved for public release; distribution unlimited.

Qualified requesters may obtain additional copies from the Defense Documentation Center; all others should apply to the Clearing House for Federal Scientific and Technical Information.

Table of Contents

I.	Summary.....	i
II.	Research Report	
A.	Crystallization of Amorphous Silicon (F.J. von Preissig).....	1
B.	Interaction of Phosphosilicate Glass with Water (F.J. von Preissig).....	13
C.	A Model of Void Growth in Encapsulated Metal Lines (Anne I. Sauter).....	35
D.	The Effect of Oxygen on the Thermal Stability of $Si_{1-x}Ge_x$ Strained Layers (D.B.Noble).....	55
III.	Oral Presentations Resulting from AFOSR Grants No. 89-0185 and 86-0051....	68
IV.	Publications Resulting from AFOSR Grants No. 89-0185 and 86-0051.....	69

I. SUMMARY

This program constitutes a fundamental study of the mechanical properties of microelectronic thin film materials. The work is supported by AFOSR Grant No. 89-0185. We are interested in the microscopic processes that lead to stresses in microelectronic thin films and control the mechanical properties of these materials. Our work ranges from studies of interconnect metals, passivation glasses and heteroepitaxial thin film semiconductors.

During the past year we have used the laser scanning, wafer curvature technique to study the kinetics of crystallization of amorphous silicon. When a thin film of amorphous silicon crystallizes, it also densifies and that causes the tensile stresses in the layer to increase. These stresses in turn cause the substrate on which the amorphous layer is deposited to bend. This bending can be detected by the laser scanning technique. Thus it is possible to measure the development of stresses in the film and the kinetics of the crystallization process. We find the tensile stress in the film to increase by about 500 MPa when crystallization occurs. This is a very large stress that could have significance for device processing and applications. By measuring the kinetics of this stress change at different temperatures we have been able to measure the activation energy for the crystallization process. We find an activation energy of about 3 eV. This compares favorably with other measurements of the kinetics of the amorphous to crystalline transformation in silicon. We expect these results to have relevance to the kinetics of regrowth of amorphized silicon layers.

We completed our work on the diffusion of water in phosphosilicate glass (PSG) films during the past year. As reported previously, the swelling associated with the sorption of water into a glass film causes compressive stresses to develop within the film. The measurement of these stresses as a function of time and at different temperatures permits a study of the kinetics of the water diffusion process. We have measured the diffusion of water into and out of PSG at different temperatures, for different phosphorous contents and for different structural states of the glass. For a sorption experiment on an initially dry glass film, the apparent activation energy for diffusion is found to range from 0.40 to 0.45 eV for different P contents. By comparison, the kinetics of desorption is very much slower. We find that water diffusion in PSG can be treated phenomenologically as if the diffusion coefficient were concentration dependent, with the diffusivity increasing with increasing water content. Alternatively, diffusion of water in the glass appears to be faster if some water is already present in the glass, perhaps indicating that monomolecular water layers are present on the "internal surfaces" in the glass and that these layers provide easy paths for diffusion of additional water.

Failure processes that occur in patterned thin films depend sensitively on the distribution of stress in these structures. During the past year our finite element study of stresses in patterned structures was extended to passivated structures and to metal lines that are permitted to deform by both elastic and plastic deformation. We find that the stresses in these structures depend sensitively on the dimensions and properties of the passivation materials and on the constitutive behavior of the metals involved. We have also developed a model of interconnect metal cracking during the past year. The model envisions a small void in a metal line that is capable of growing by diffusion. We consider that matter diffuses along grain boundaries from the void to distant parts of the line where hydrostatic tension stresses are present. The model gives a good account of many of the characteristics of metal cracking that have been reported in recent years. In particular, it predicts that the failure time for a given metal line depends strongly on temperature, on the hydrostatic stress in the line (or equivalently on the difference between the passivation temperature and the actual temperature) and on the grain size.

Our work on misfit dislocations during the past year has been focussed on methods for inhibiting the formation of misfit dislocations. We have shown that unstrained silicon capping layers greatly inhibit the formation of misfit dislocations in Si-Ge heteroepitaxial thin films. We have also found that RSP Si-Ge layers typically contain large amounts of oxygen and that the dissolved oxygen present greatly inhibits the dislocation glide processes that are involved in the formation of misfit dislocations. MBE grown Si-Ge layers typically contain much smaller amounts of oxygen and consequently are much more susceptible to misfit dislocation formation. A special effort was made to grow RSP Si-Ge layers with low oxygen contents; the resulting films were, like the MBE films, much more susceptible to misfit dislocation formation. These results strongly suggest that solid solution strengthening by oxygen (or perhaps by nitrogen) represents an effective method for inhibiting the formation of misfit dislocations in heteroepitaxial structures.

The presentations and publications that have resulted from this work are listed at the end of this report. Three Ph.D. degrees will be granted under this program in the coming year.

II. RESEARCH REPORT

A. Crystallization of Amorphous Silicon

F.J. von Preissig (Graduate Research Assistant)

1. Introduction

Phase transformations and related structural changes in thin solid films constitute a rich and technologically important area of study. As is well known, a density change associated with a thin-film transformation results in a stress change. Under the right circumstances, it should be possible to derive information about the kinetics of the transformation by monitoring film stress as a function of time and temperature. This idea has been applied to the crystallization of TaSi₂ and WSi₂ films with some success.[1]

Another transformation of interest is the conversion of amorphous silicon (a-Si) to polycrystalline silicon (polysilicon). This transformation occurs by a nucleation-and-growth process that is interface-controlled, rather than diffusion-controlled, since no compositional changes are involved. Atoms in amorphous silicon are mostly four-fold coordinated, as in crystalline silicon, but bond-angle and bond-length distortions result in a lack of long-range order.[2] The strain energy of these distortions drives the crystallization reaction.[3] This reaction has previously been examined using X-ray diffraction,[4,5] transmission electron microscopy,[6,7] and electrical conductivity measurements.[8] The kinetics and growth morphology were found to depend on film-formation conditions, impurity content, underlying material, and film thickness. Polysilicon formed from a-Si has better electronic mobility and a smoother surface than deposited polysilicon and is produced at temperatures compatible with glass substrates, making it a good material for the active region of thin-film transistors (TFTs).[6,9] TFTs are used for large-area applications such as liquid-crystal displays and image sensors, and they have potential use in three-dimensional ICs.

This report briefly explores the feasibility of using stress measurement as a tool to study a-Si crystallization and other thin-film transformations. The experiments described are an application of the high-temperature capabilities of the stress-measurement system.

2. Theory

Crystallization Kinetics

The kinetics of solid-state transformations that occur by a process of nucleation and growth of a reorganized form of material in the original material is a long-studied area of materials science. Isothermal transformations are often described phenomenologically by the Avrami equation [10]

$$X = 1 - \exp(-Kt^N), \quad (1)$$

where X is the fraction of material transformed, t is time, and K and N are constants that depend on the nucleation rate, the velocity of the interface between transformed and untransformed regions, and the growth morphology. If the process is not dependent on long-range diffusion, then $3 \leq N \leq 4$ for three-dimensional growth and $2 \leq N \leq 3$ for two-dimensional growth. The lower number of these ranges corresponds to the case of a constant number of nuclei, the upper to the case of a constant nucleation rate per untransformed volume. Crystallization in a thin film would approximate a two-dimensional process if the final grain size were much larger than the film thickness. The derivation of Eq. (1) is based on the following assumptions: nuclei exist at spatially random locations, the nucleation rate per untransformed volume is constant or decreases with time, and the interface velocity is constant, but not necessarily isotropic. Equation (1) yields a sigmoidal (S-shaped) X -versus- t curve. Sometimes it is necessary to replace t in this equation with $t - t_0$, where t_0 is the *incubation time*.[11] The incubation time is roughly defined as the time it takes for the first stable nuclei to form, and it is often inversely proportional to the nucleation rate.

Crystallization Stress Changes

For an amorphous-to-crystalline transformation of a thin film in which no plastic deformation takes place, we can write

$$\varepsilon_c - \varepsilon_a = \frac{1}{3} \frac{\rho_c - \rho_a}{\rho_a}, \quad (2)$$

where e is biaxial strain, r is density, and the subscripts "c" and "a" stand for crystalline and amorphous, respectively. The stresses in the fully amorphous and crystalline films are

$$\begin{aligned}\sigma_a &= B_a \epsilon_a \quad \text{and} \\ \sigma_c &= B_c \epsilon_c ,\end{aligned}\tag{3}$$

where B is the biaxial modulus. Unless the individual grains in the polycrystalline film are all oriented with the same polysymmetric axis of elastic symmetry perpendicular to the substrate, the stresses may vary from grain to grain and with direction in a grain, with s_c and B_c in Eqs. (3) being average values. (The silicon films in this study are known[5] to crystallize with a very dominant (111) orientation, so the conditions of uniformity and polysymmetry are satisfied.) The stress change resulting from the complete transformation is

$$\Delta\sigma_{\text{total}} = \sigma_c - \sigma_a .\tag{4}$$

For partially crystallized films, we will make the assumption that the local stresses in the amorphous and crystalline regions are given by Eqs. (3). Then the average (measured) stress is

$$\begin{aligned}\sigma &= (1-X)\sigma_a + X\sigma_c \\ &= \sigma_a + X\Delta\sigma_{\text{total}} .\end{aligned}\tag{5}$$

Hence,

$$\Delta\sigma \equiv \sigma - \sigma_a = X\Delta\sigma_{\text{total}} ,\tag{6}$$

i.e., the measured stress change at any point in the transformation is proportional to the fraction of material transformed. Thus, stress measurement can be used to monitor crystallization through Eq. (6) if there is a sufficient density change, there are no other sources of stress change, and the assumption about local stresses is approximately correct. Other kinds of transformations could be treated similarly.

The density change associated with the transformation is [from Eqs. (2) and (3)]

$$\frac{\rho_c - \rho_a}{\rho_a} = 3(\epsilon_c - \epsilon_a) = 3\left(\frac{\sigma_c}{B_c} - \frac{\sigma_a}{B_a}\right) .\tag{7}$$

3. Experiments

A film of non-hydrogenated amorphous silicon 1000 Å thick was deposited onto a silicon wafer having 730 Å of thermal oxide by low-pressure chemical vapor deposition (LPCVD) at 570°C using pure SiH₄. (The deposition was done by Xerox PARC personnel.) The wafer was then cut into standard-size samples. After the stress-system furnace was pre-heated to 580°, 600°, or 620°C, samples were inserted and stress changes were measured over time on argon.

The stress changes are shown in Fig. 1. The data curves are quite smooth, in spite of the measurements having been made on very thin films at high temperatures. The stress moves in the tensile direction as the transformation proceeds, indicating that the polycrystalline form of silicon is denser than the amorphous form. A small amount of post-transformation stress change is visible, but its rate is so small that the stress relaxation occurring during the transformation can probably be safely ignored. The value of Ds_{total} for each of the curves is near 506 MPa. We can use this information to roughly quantify the density change using Eq. (7). If we assume that s_a is zero (this may be reasonable since there should be negligible thermal stress), then s_c equals 506 MPa and we do not need to know B_a . Taking B_c as the value (2.14×10^{-5} MPa) for (111)-Si at 600°, Eq. (7) yields a density increase of 0.7%. The actual value of B_c is probably smaller than assumed due to the presence of grain boundaries, making the actual density change proportionally larger than calculated.

Assuming that the stress change is proportional to X in accordance with Eq. (6), the sigmoidal form of the curves in Fig. 1 is expected. The transformation rate at first increases with time as the total amorphous-crystalline interface area increases, then decreases due to the impingement of growing crystallites with each other and with the film boundaries, and finally approaches zero as the transformation approaches completion.

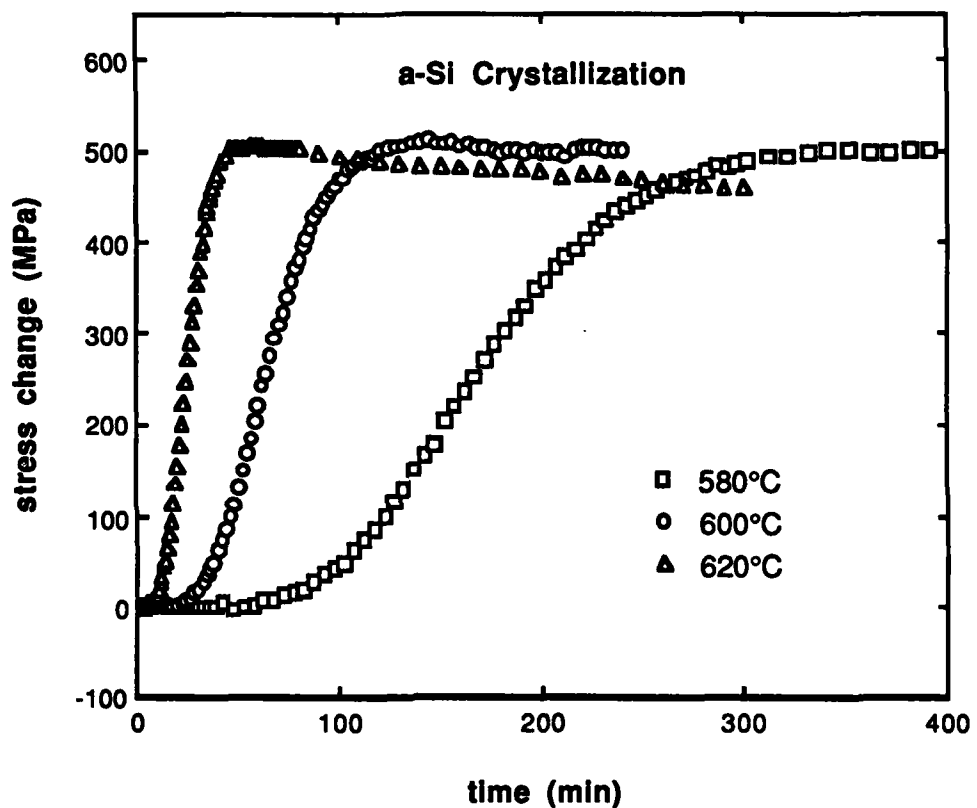


Fig. 1 Stress changes associated with the crystallization of amorphous-silicon films at three different temperatures. Film thickness is 1000 Å.

The rate of transformation increases with temperature. In order to quantify the effect of temperature on transformation rate, the times for $X = 10\%$, 50% , and 90% were noted for each temperature. The reciprocals of these times, or of the differences between them, are measures of transformation rate and are shown plotted in Arrhenius form in Fig. 2. The incubation period, if one exists, is included in $t_{10\%}$ but not in the time differences. The activation energy for post-incubation transformation is given by both $(t_{50\%}-t_{10\%})^{-1}$ and $(t_{90\%}-t_{10\%})^{-1}$ as 3.06 eV. This is in close agreement with the value, 3.2 eV, obtained for this material by X-ray diffraction measurements.[5] The larger effective activation energy for $t_{10\%}^{-1}$ suggests that an incubation period exists and that the activation energy associated with it is higher than that of the post-incubation transformation. This notion is in general agreement with X-ray results that give an activation energy of 3.9 eV for t_0^{-1} .[5] This quantity is probably the activation energy for nucleation. The activation energy (3.06 eV) associated with transformation, however, cannot be ascribed to a single physical process since it is affected by differences in the number of nuclei as well as by differences in interface velocity. For comparison, the activation energy for (100)-epitaxial regrowth of silicon amorphized by ion implantation has been reported as 2.7 eV.[3]

The three transformation curves have in a sense the same shape, as illustrated in Fig. 3. Here time has been transformed by linear functions so that $t_{10\%}$ and $t_{50\%}$ coincide for each temperature. When this is done, the entire curves (after incubation) superimpose almost exactly. This property indicates that the ratio of crystallization rates for two temperatures at a given extent of transformation is constant over the whole transformation. It is the reason that $E = 3.06$ eV was obtained the two different ways.

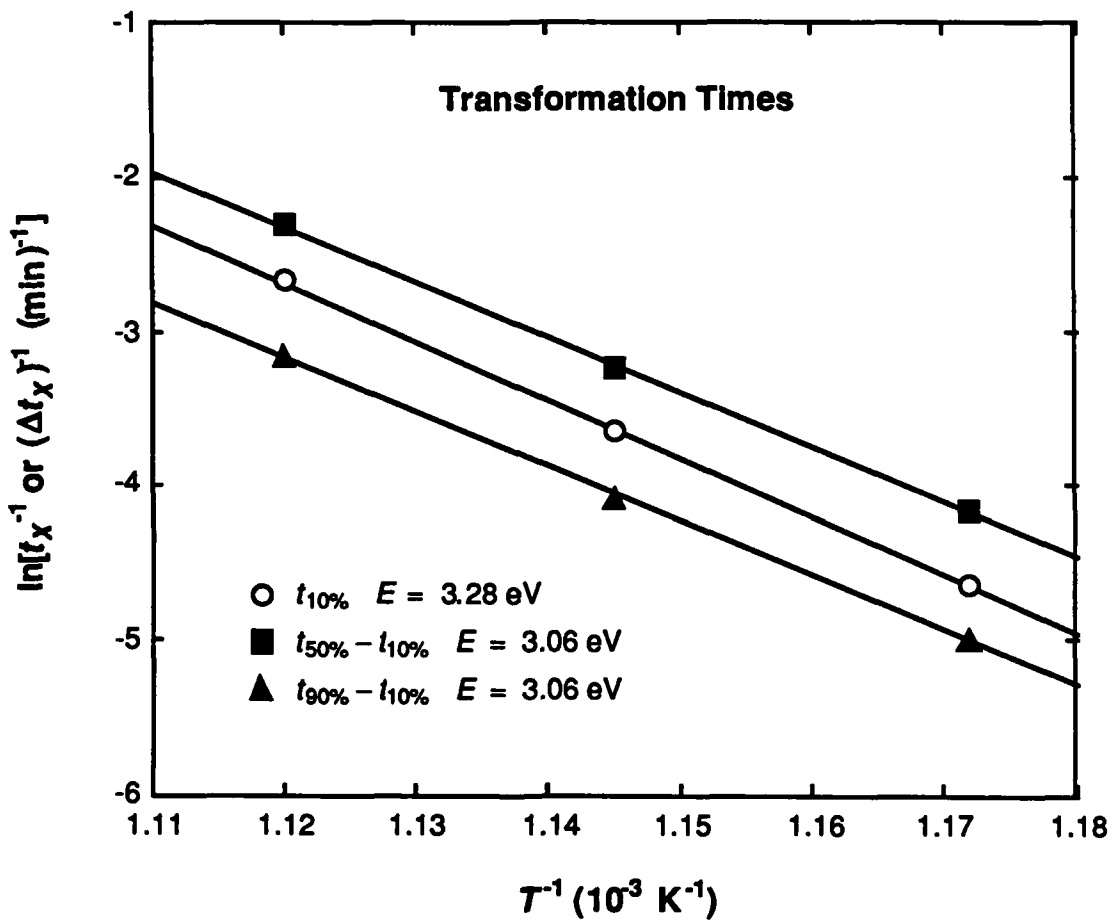


Fig. 2 Arrhenius plot of reciprocal transformation times for a-Si crystallization, from the data of Fig. 1. t_X = time at which fraction X of the material is transformed. E = activation energy.

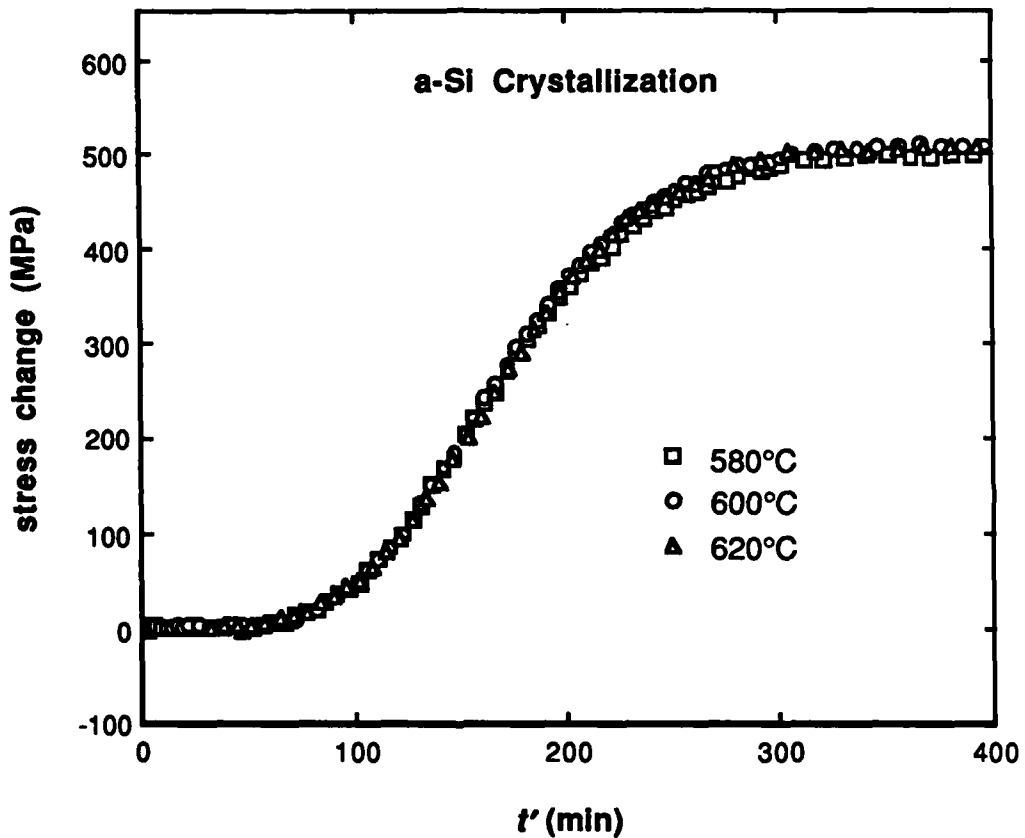


Fig. 3 Curves of Fig. 1 made to superimpose by the application of a linear function ($t' = c_1t + c_2$) to the time variable for each temperature.

According to the Avrami equation including incubation [Eq. (1) with $t \rightarrow t - t_0$], a plot of $\ln \ln[(1 - X)^{-1}]$ versus $\ln(t - t_0)$ is a line with slope N . Figure 4 shows the data for the 580° crystallization experiment, for $X = 2\%$ to $X = 98\%$, plotted in this way. But t_0 is unknown since it is not possible to determine $t_{X=0}$ accurately from the data, and there is some uncertainty about the effect of the initial thermal transient. The incubation time is assumed to be zero for one of the curves and 40 minutes for the other. The line fitted through the $t_0 = 0$ curve yields an effective value of 3.42 for N , but the curve is not very linear, its slope varying from about 2.4 to 4.2. Using $t_0 = 40$ gives approximately the most linear plot, with an average slope of 2.45. For this curve, the slope is about 2.0 at the ends and has a maximum value of 2.6. We may conclude from this analysis that uncertainty in t_0 precludes accurate determination of the constant N and that the data does not behave in close accordance with the Avrami equation. In fact, the Avrami equation would not be expected to apply to this case since the average grain size is known[5] to be roughly 2000 Å, which is neither much smaller than h (1000 Å) (3-D growth) or much larger than h (2-D growth). But the lack of applicability of the Avrami model does not invalidate the comparison of transformation rates using the stress data.

4. Recommendations for Future Work

Elastic relaxation at the boundary between regions having different stress would affect stresses near the boundaries, compromising our assumption about local stresses having either a "transformed value" or an "untransformed value." A more sophisticated model relating measured stress change to fraction transformed that takes this into account should be formulated. Also, models could be corroborated by other methods, such as TEM and conductivity measurements.

More can be learned about transformation kinetics if nucleation and subsequent growth can be analyzed separately. One way to do this would be to make extensive use of microscopy, but this defeats the objective of having an analytical technique that is easy to use. In some material systems, it may be possible to control nucleation so that growth processes can be analyzed. Ion implantation has been used to inhibit nucleation in a-Si films.[5] If small selected areas are shielded from this implantation, these areas should crystallize first and serve as artificial "nuclei" for subsequent lateral growth.

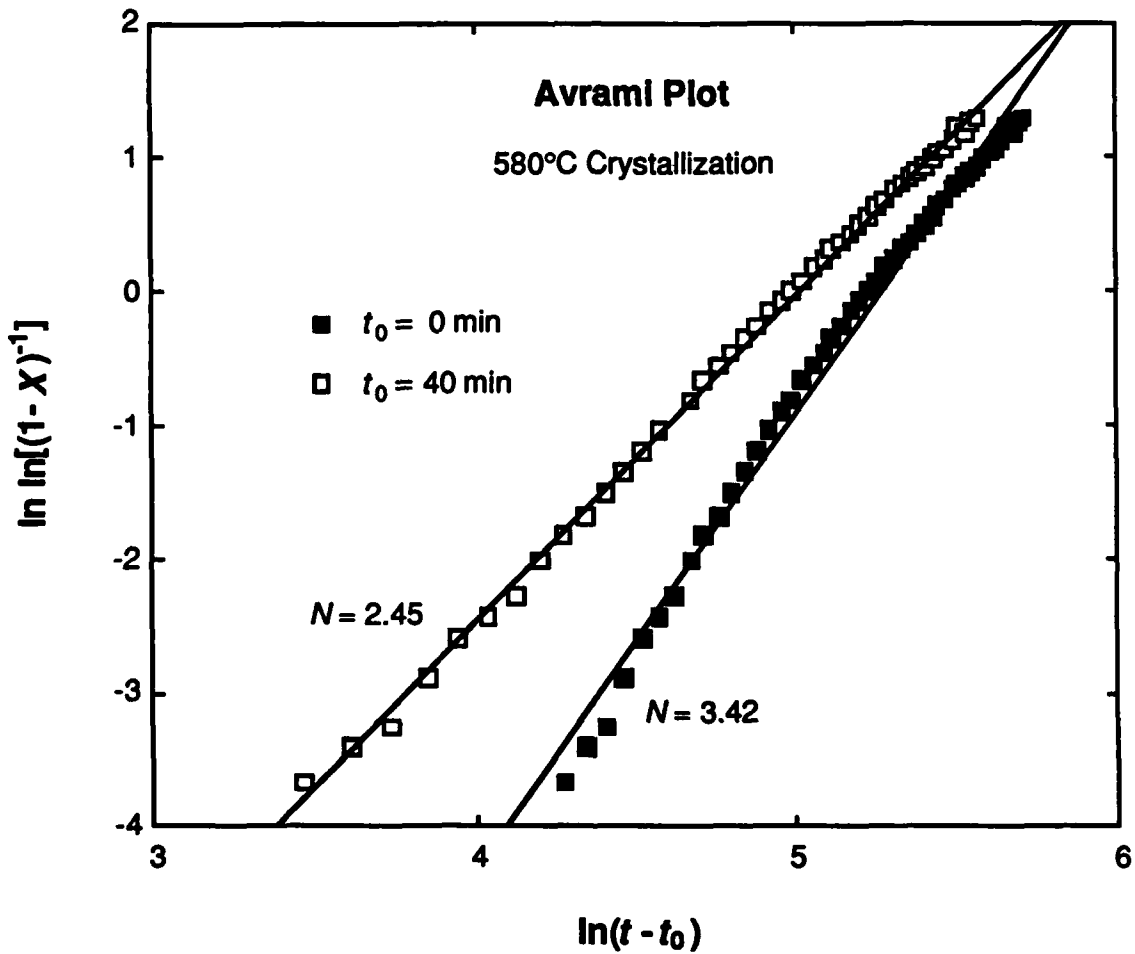


Fig. 4 a-Si crystallization data plotted in a manner that would result in a straight line with slope N if the equation $X = 1 - \exp[-K(t - t_0)^N]$ were satisfied, for two different assumed values of t_0 . X = fraction transformed, t = time, t_0 = incubation time, and K and N are constants.

Measurement of film stress as a function of temperature using substrates having different CTEs can be used to calculate the biaxial modulus of films.[12] Applied to films before and after transformation, this technique could yield values of B for use in calculating density changes by Eq. (7).

5. Summary

The process of crystallization in amorphous-silicon thin films was monitored by *in-situ* stress measurement, based on a model in which the measured stress change is proportional to the fraction of material transformed. The density increase accompanying this phase change was determined to be about 1%. Comparing transformation rates at different temperatures yields an activation energy for post-incubation growth of 3.06 eV and provides evidence for an incubation process having a higher activation energy. The kinetics of the transformation does not appear to follow the Avrami model well. The stress technique has proved to be a convenient method for monitoring the kinetics of a-Si crystallization, and it could be applied similarly to the study of other thin-film transformations. However, the technique does not by itself yield very specific information about transformation mechanisms, and its theoretical underpinnings could be improved.

6. References

1. P. H. Townsend, *Inelastic Strain in Thin Films* (Ph.D. dissertation, Dept. of Materials Science and Engineering, Stanford University, 1987), Chap. 6.
2. N. F. Mott and E. A. Davis, *Electronic Processes in Non-Crystalline Materials*, second edition (Clarendon, Oxford, 1979), Chap. 7.
3. G. L. Olson and J. A. Roth, "Kinetics of solid phase crystallization in amorphous silicon," *Mat. Sci. Reports* 3(1), 1 (1988).
4. R. Bisaro, N. Proust, J. Magariño, and K. Zellama, "Crystallization study of chemically vapour-deposited amorphous silicon films by *in-situ* X-ray diffraction," *Thin solid films* 124, 171 (1985).
5. I.-W. Wu, A. Chiang, M. Fuse, L. Öveçoglu, and T.-Y. Huang, "Retardation of nucleation rate for grain size enhancement by deep silicon ion implantation of low-pressure chemical vapor deposited amorphous silicon films," *J. Appl. Phys.* 65(10), 4036 (1989).

6. M. K. Hatalis and D. W. Greve, "Large grain polycrystalline silicon by low-temperature annealing of low-pressure chemical vapor deposited amorphous silicon films," *J. Appl. Phys.* **63**(7), 2260 (1988).
7. R. B. Iverson and R. Reif, "Recrystallization of amorphized polycrystalline silicon films on SiO₂: temperature dependence of the crystallization parameters," *J. Appl. Phys.* **62**(5), 1675 (1987).
8. R. Bisaro, J. Magariño, K. Zellama, S. Squelard, P. Germain, and J. F. Morhange, "Solid-phase crystallization kinetics in doped *a*-Si chemical-vapor-deposition films," *Phys. Rev. B* **31**(6), 3568 (1985).
9. I.-W. Wu, A. G. Lewis, T.-Y. Huang, and A. Chiang, "Performance of polysilicon TFT digital circuits fabricated with various processing techniques and device architectures," *SID Int'l. Symp. Tech. Digest* (1990), pp. 307-310.
10. J. W. Christian, *The Theory of Transformations in Metals and Alloys*, second edition, Part I (Permagon, Oxford, 1975), Chaps. 1 and 12.
11. P. Cotterill and P. R. Mould, *Recrystallization and Grain Growth in Metals* (J. Wiley & Sons, New York, 1976), pp. 44-45.
12. T. F. Retajczk, Jr. and A. K. Sinha, "Elastic stiffness and thermal expansion coefficient of BN films," *Appl. Phys. Lett.* **36**(2), 161 (1980).

B . Interaction of Phosphosilicate Glass with Water
F.J. von Preissig (Graduate Research Assistant)

1. Introduction

Phosphosilicate glass (PSG) and other silicate glasses are materials that have numerous uses in IC technology.[1,2] Deposition methods and properties of these films have long been subjects of active study.[3-5] In integrated circuits, PSG is typically used in two forms. At its lowest level in the IC structure, it is deposited and then annealed at about 1000°C to fuse and flow the material. The resulting layer is intended to insulate electricity-conducting structures from each other and provide a surface smooth enough to ensure the continuity of subsequently deposited conductor lines. This layer is also a getterer of harmful alkali ions and provides other forms of chemical protection. At higher levels, above nonrefractory conductor materials such as aluminum, the glass has the same insulating and protecting roles but must remain unfused. The uppermost glass layer has the additional function of providing mechanical protection to the underlying circuitry, especially during chip separation and packaging operations. Borophosphosilicate glass (BPSG) is increasingly replacing PSG in some applications, due to BPSG's lower flow temperature, lower stress (as deposited), and favorable etch-rate characteristics.[6]

Although PSG is used to provide protection against contaminants in ICs, in its unfused form it does not guard well against the negative effects of water. Water easily penetrates plastic packaging, picking up other contaminants, and may then pass through cracks and other defects in an outer silicon nitride passivation layer.[7] Some water may already be inside as a by-product or contaminant of the fabrication process. Water diffuses fairly easily through PSG layers, under some conditions[8] leaching out phosphorus to form phosphoric acid. The corrosion of conductor lines by phosphoric acid and by other

mechanisms[9] involving the water molecule is a significant reliability problem. The presence of water can also cause metal deposition problems,[10] threshold voltage shifts and transconductance degradation in MOSFETs,[11] and stress-corrosion cracking of glass.[12] Because of these potential problems, there is technological motivation for studying the interaction of PSG and related materials with water.

Soon after investigators began measuring stresses in deposited films of SiO₂ and other silicates, they noticed a reduction in tensile stress over time, sometimes leading to compression, when the films were exposed to air or other humid environments.[13-16] The stress change was accompanied by an increase in water and hydroxyl (OH) content, and it was found to be at least partially reversible in dry environments and at elevated temperature. The phenomenon can be described as a swelling of the film, constrained in two dimensions by the substrate, due to the sorption of water into the film. After a high-temperature fusion treatment, film density increases by several percent [8,17] and water penetration is almost completely inhibited,[8] indicating that porosity of the as-deposited films is what allows the sorption to occur. (Here "porosity" is taken to mean an openness of structure in some sense.) The pores are apparently too small to be imaged clearly, however, in optical or electron micrographs of IC structures. Expansion of bulk samples of a very porous glass (Vycor) occurring with sorption of water has been examined.[18] This expansion was attributed to a "spreading pressure" acting on the surfaces of the pores and resulting from energy decreases associated with the adsorption of molecules.[19] In thin films also, swelling may be due to internal-surface-energy lowering, but the phenomenon has also been attributed to a breakdown of the silicate structure due to the formation of silanol (Si-OH) groups.[13] Although the exact mechanism is not known, it is clear that water can be absorbed into PSG films and that this process causes the film stress to change in the compressive direction. It should therefore be possible to monitor the sorption process under different conditions and as a function of time by measuring stress,

provided all other sources of stress change are inhibited or accounted for. This report describes experiments in which aspects of PSG-water interaction were inferred from changes in film stress as a function of time, temperature, ambient gas, phosphorus content, and pre-annealing conditions. The diffusivity of water in PSG was the principal object of the experiments, but sorption and desorption behavior helped shed additional light on the chemistry of the interaction and on the structure of PSG as well.

2. Diffusion Model

The model used to analyze sorption of water into the PSG films is presented here. As illustrated in Fig. 1, a film of thickness h is attached to an impermeable substrate. The initial concentration of diffusant (water) is uniform through the film. At time zero the concentration at the surface ($u = 0$) is reset to a new level based on chemical equilibrium with a changed environment, and is held constant. The concentration profile changes until ultimately the diffusant concentration is again uniform, at the new level. The total amount of diffusant in the film at a given time is called m . The diffusion coefficient, D , is assumed in this model to be constant. Under these conditions, the way in which m changes over time is given by the equation[21]

$$\frac{m(t) - m(0)}{m(\infty) - m(0)} = 1 - \frac{8}{\pi^2} \sum_{i=1}^{\infty} (2i-1)^{-2} \exp\left\{-\left[\frac{(2i-1)\pi}{2h}\right]^2 Dt\right\}. \quad (1)$$

If it is *assumed* that changes in film stress are proportional to water concentration, then

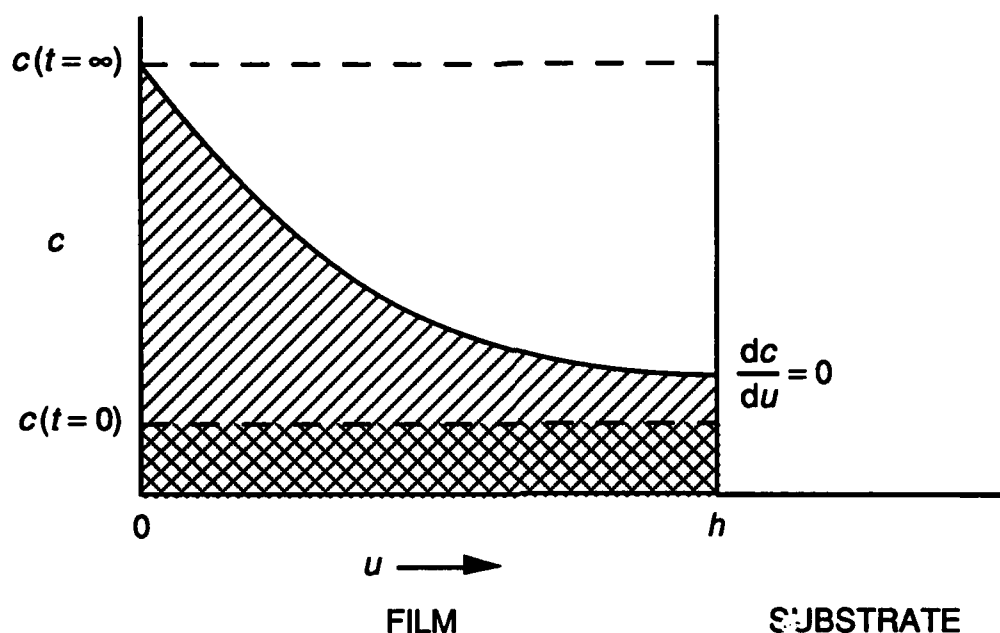
$$\begin{aligned} \frac{\sigma(t) - \sigma(0)}{\sigma(\infty) - \sigma(0)} &= \frac{\Delta\sigma}{\Delta\sigma_u} \\ &= 1 - \frac{8}{\pi^2} \sum_{i=1}^{\infty} (2i-1)^{-2} \exp\left\{-\left[\frac{(2i-1)\pi}{2h}\right]^2 Dt\right\}, \end{aligned} \quad (2)$$

where σ is the film stress, averaged over the thickness of the film, D_s is the stress change, and $D_{s\infty}$ is the stress change for the sorption reaction taken to completion. If this model is realistic, then Eq. (2) can in principle be used to calculate water diffusivities based on stress measurements made over time on films exposed to an environment that changes the equilibrium water concentration. McInerney and Flinn[22] used this technique to determine diffusivities in CVD PSG and SiO₂ films exposed to high humidity at various temperatures. Their stress measurements were made at room temperature.

3. Sorption Experiments

The model described above was applied to the analysis of sorption experiments carried out on the PSG samples. The experiments were conducted as follows: Immediately after removal from a desiccator, the nominally dry sample was measured (in most cases) for curvature at room temperature and then inserted into the furnace. The furnace was at 110°, 130°, or 150°C with argon flowing at this time. After a few minutes, enough time for the temperature of the sample to stabilize, a "time zero" curvature measurement was made and the gas was switched to steam, which flowed at about 3.5 cc/sec. Curvature was measured periodically under these conditions until approximate saturation was reached, i.e., when curvature apparently had ceased changing. These experiments were conducted at each of the three temperatures for each of the three film compositions. The films containing 5 wt% phosphorus were thinned to about 3000 Å using a buffered oxide etchant prior to drying and sorption so that saturation could be approached in a reasonable period of time.

A typical sorption result is shown in Fig. 2. Here stress is plotted versus the square root of time for a 3%-P film exposed to steam at 110°. (To compensate for delay in changing from argon to pure steam in the sample compartment, 1.3 minutes was subtracted from the time data for all experiments. This value was chosen because it smoothed out an initial tail in the



u = depth

t = time

c = concentration

$$m = \int_0^h c du$$

Fig. 1 Boundary conditions and concentration profile for a one-dimensional diffusion model used to analyze sorption in thin films.

data for all experiments.) As expected, stress moves in the compressive direction with time. The curved line represents a least-squares best fit of Eq. (2) to the data, with the initial stress, final stress, and diffusion coefficient used as fitting parameters. The data is quite smooth, and the fit is good, but not perfect. The initial linearity of the curve arises from the $t^{1/2}$ dependence of m that would proceed indefinitely for sorption into a semi-infinite medium. For a finite slab, deviation from this relation is only about 1.2% by the time half of the total change in diffusant content has occurred, but the influence of the impermeable boundary increases until eventually the material is essentially saturated and the curve becomes level.

The fitting of Eq. (2) to the sorption data yields a value of D , but since the fit is imperfect, this value would be affected by variations in the spacing of the data points. Regions denser in points would tend to fit more closely, and the relative spacing of points did differ between experiments. Another method of calculating D , still based on Eq. (2) but independent of point spacing, was used in order to yield more consistent values. With the time at which D_s/D_{s_0} equals 1/2 defined as $t_{1/2}$, Eq. (2) gives D as

$$D = 0.197 h^2 / t_{1/2} . \quad (3)$$

D_s was known from experiment since the sorption reaction was taken essentially to completion, well past times at which $D_s/D_{s_0} = 99\%$ for the fitted curve. To get $t_{1/2}$ from the data, a central region of data was fit with a polynomial equation for smoothing and interpolation, and $t_{1/2}$ was evaluated from this equation. Insertion of experimental $t_{1/2}$ values into Eq. (3) yields effective diffusion coefficient values.

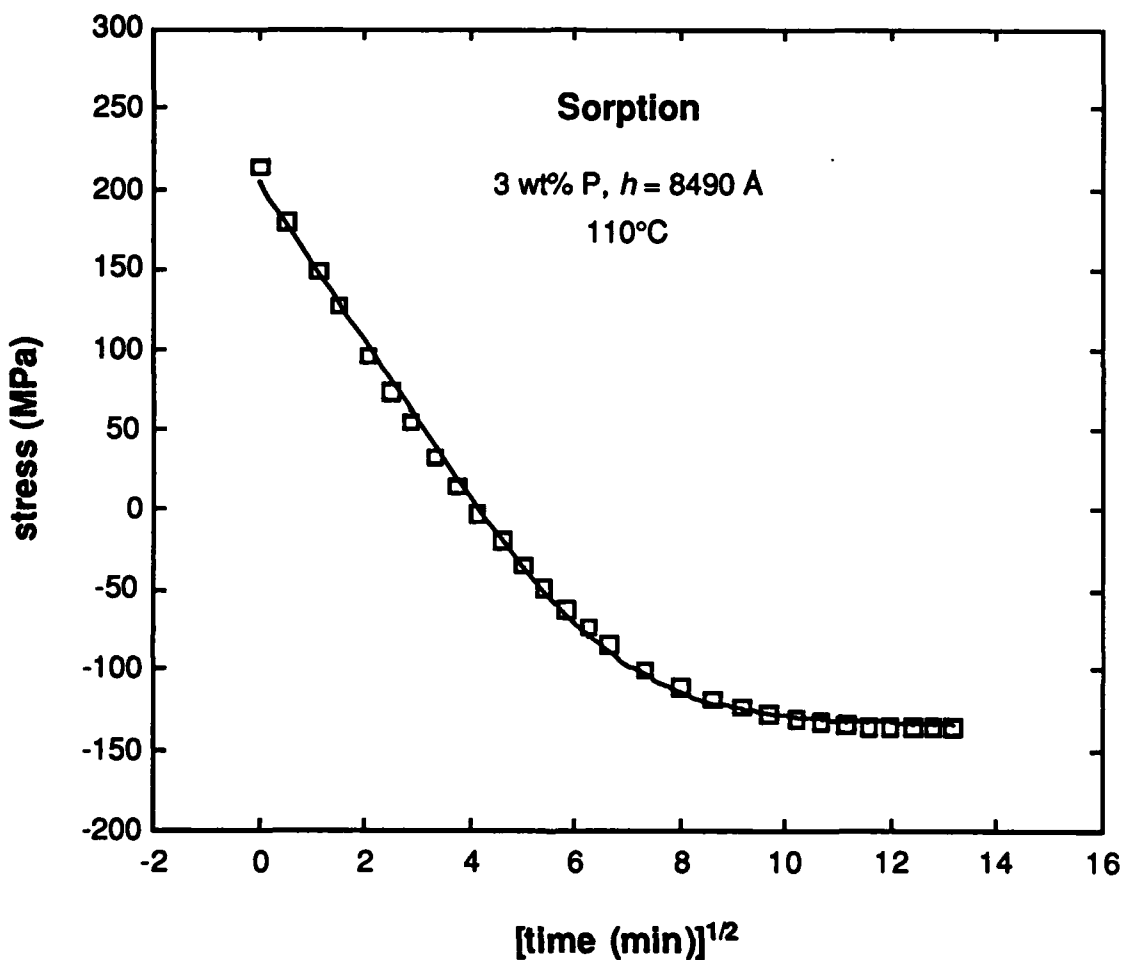
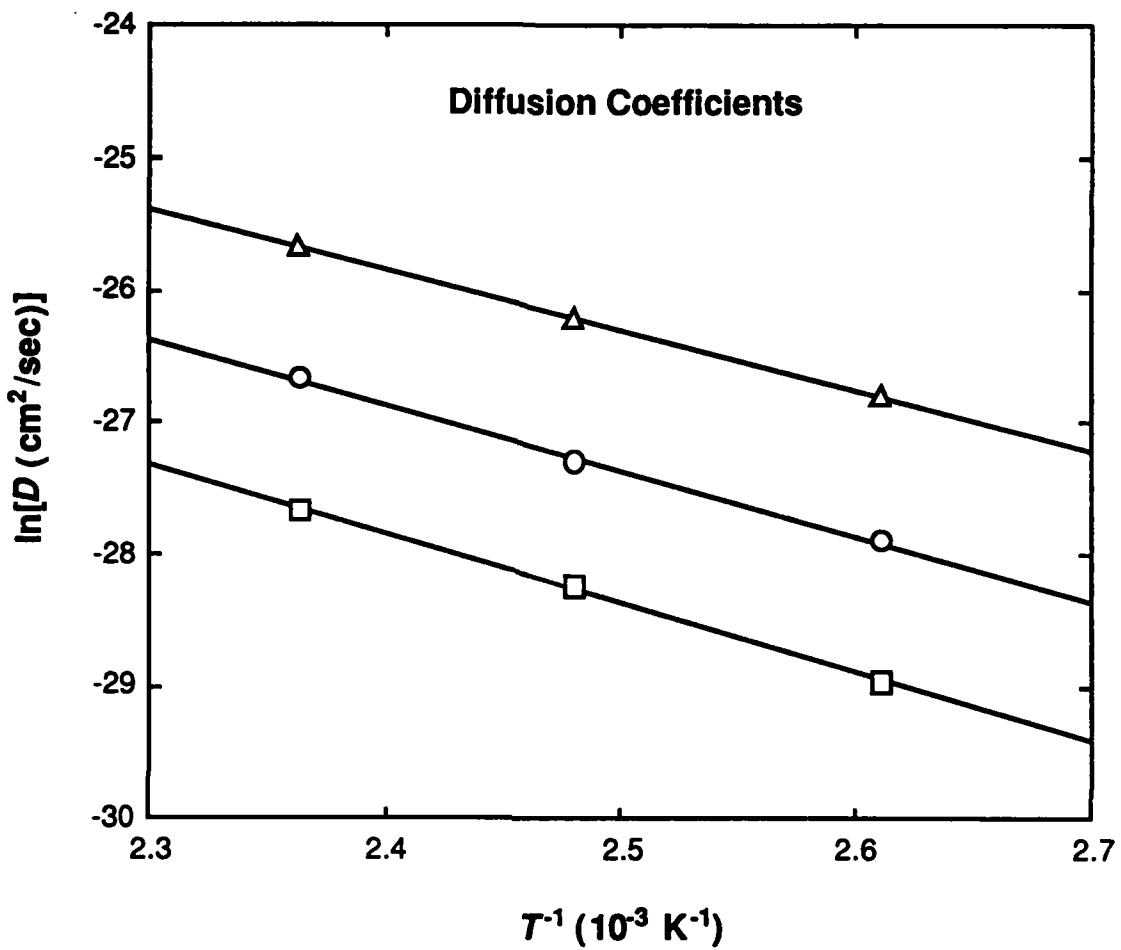


Fig. 2 Stress versus square root of time for a film exposed to steam in a sorption experiment. Squares are data points. The solid line is a fit of Eq. (2) to the data.

The diffusion coefficients obtained by this method are displayed in an Arrhenius plot in Fig. 3. Diffusivity increases by a factor of roughly 1.8 per 20° temperature increase, and it decreases by a factor of approximately 2.8 (at 130°) per 1% increase in phosphorus content. Although the temperature range is small, the data seem sufficiently well-behaved to extract activation energies for each film composition using the fitted lines. The calculated activation energies vary from 0.40 eV to 0.45 eV, increasing slightly with phosphorus content. These energies are fairly low compared to those of other diffusive processes in solids, probably indicative of the ease of passage of water molecules through the pores in the glass. Other reported activation energies for water diffusion in PSG range from 0.41 eV to 0.52 eV.[22,23] For comparison, the activation energy for the parabolic rate constant (diffusion controlled) for thermal oxidation of silicon in wet oxygen is 0.71 eV.[24] Perhaps relevant to porous-glass diffusion is the isosteric heat of adsorption of water onto silica surfaces, reported as 0.57 eV/molecule at low surface coverages and 0.46 eV at high surface coverages.[25] The decrease in D with increasing % P correlates with a known density increase with % P for as-deposited PSG films,[3,20] which in turn is likely related to the viscosity-lowering function of phosphorus and other elements added to SiO₂.[26]

One hypothesis for explaining the correlation between diffusivity and density is as follows: Imagine the PSG structure as a distribution of pores (bubbles, gaps, tunnels, etc.) of various sizes contained in a dense matrix material. Much of the water resides in the larger pores, but movement between these pores occurs through constricted interconnections



	<u>wt% P</u>	<u>E(eV)</u>	<u>$D_0 (10^7 \text{ cm}^2/\text{sec})$</u>
Δ	3	0.40	3.88
○	4	0.43	2.97
□	5	0.45	2.88

Fig. 3 Arrhenius plot of diffusion coefficients, obtained by the sorption-stress method, of water in PSG films. E = activation energy, D_0 = preexponential factor. Experiment temperatures are 110°, 130°, and 150°C.

between them. The energy required for a water molecule to squeeze through the constrictions is higher for smaller constrictions. The experimentally measured activation energy would be an average of such energies. Now, in a denser structure, the average interconnection diameter is smaller, resulting in a higher activation energy. Furthermore, there are fewer passageways large enough to allow water to pass through them at all. This decrease in the opportunities for travel for a water molecule could cause the preexponential factor, D_0 , to be lower, as was observed. In classical models of diffusion,[27] D_0 is proportional to the molecular vibration frequency, which would not be affected by density, and to the *fraction* of diffusant molecules that are in a position to make a traveling jump. Hence, if densification affects porosity in such a way that interconnection passability decreases relative to water concentration, D_0 decreases. This seems realistic; densification could pinch off a large number of already-small constrictions while having relatively small effect on the total surface area available for adsorption of water molecules.

4. Annealing Effects

A set of samples with films containing 3 wt% P were annealed at 430°C (also the deposition temperature) in argon before undergoing sorption tests in steam at 150°. The diffusion coefficients obtained are shown plotted in Fig. 4. Diffusivity decreases as a function of annealing time, rapidly at first and by a factor of 2.6 for the 30-minute anneal. This suggests that the deposition rate and deposition-furnace residence time, which were carefully controlled in this study, would have a significant effect on film diffusivity.

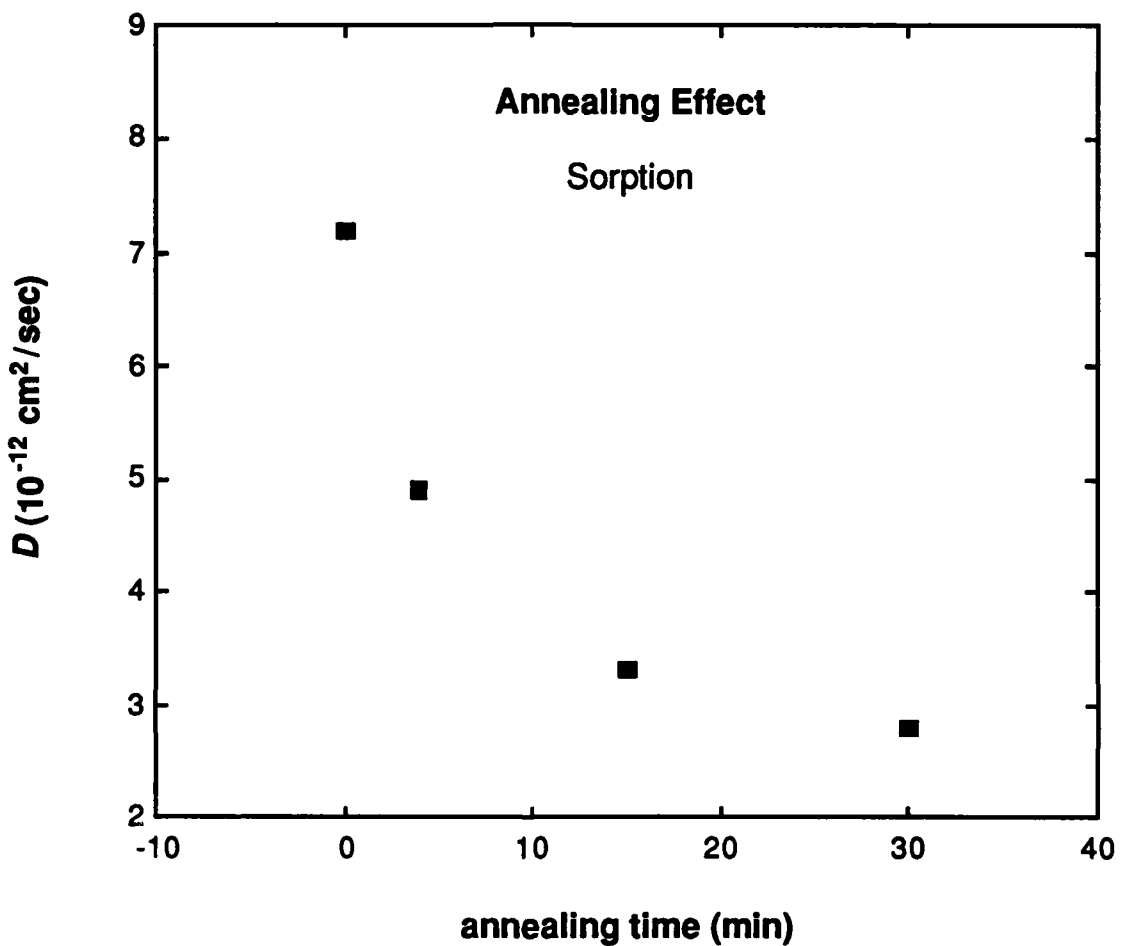


Fig. 4 Diffusion coefficients obtained from sorption experiments at 150°C on films first annealed at 430°C. The film contained 3 wt% phosphorus.

5. Desorption Experiments

Figure 5 shows what happened when a 3%-P film, saturated in steam at 110°C, was exposed to pure argon at the same temperature. As water desorbs, the stress changes in the tensile direction. Under the assumptions of the diffusion model, the stress changes for sorption should have exactly the same time dependence [given by Eq. (2)] as those for the corresponding sorption experiment. But a best fit of the diffusion equation to the sorption data does not fit well at all. The experimental curve can be described as "rounder" than the equation curve (and sorption curve). The experimental curve has an initial linear regime, but it is shorter. A "saturation" level, if it exists, is not approached as sharply. Other differences between sorption and desorption behavior are illustrated in Fig. 6. The speed of reaction, and apparently the ultimate stress change, are dramatically different, even though the temperature is the same. The sorption curve reaches approximate saturation in about 2.5 hours, but after 82 hours the desorption curve has still not leveled off. Even so, the desorption curve seems to be approaching some stress level much lower than the initial dry state.

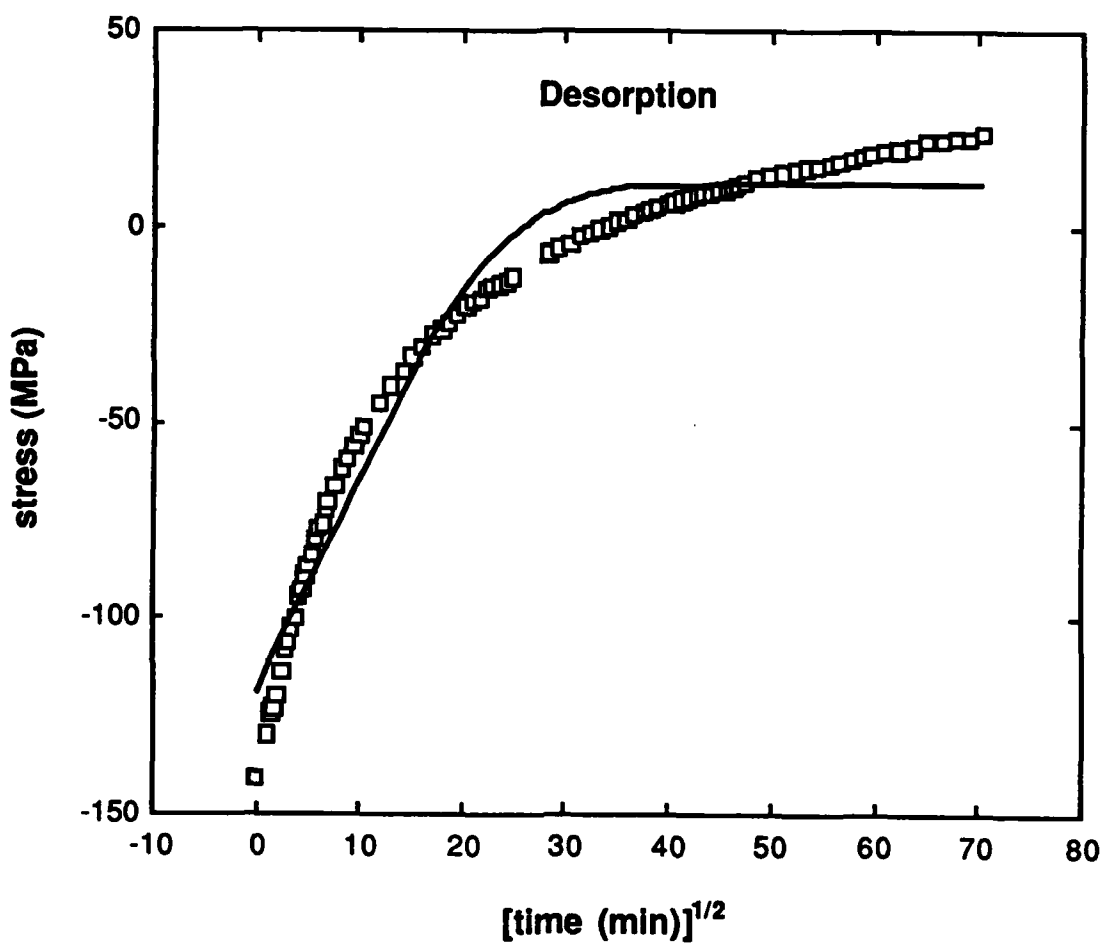


Fig. 5 Desorption behavior of a previously saturated film (3 wt% P) in an argon ambient at 110°C. The solid line is a best fit of Eq. (2).

These differences can be explained qualitatively by invoking the idea of a concentration-dependent diffusion coefficient. Figure 7 shows sorption (A) and desorption (C) curves (from Ref. 21) computed on the basis of a diffusion coefficient that increases exponentially with concentration, along with the curve (B) corresponding to Eq. (1). As with the experimental data, the variable- D desorption curve is rounder and less steep than the constant- D curve. The variable- D sorption curve, on the other hand, has a larger linear regime and is steeper. These comparative features hold for *any* monotonically increasing D -versus- c function.[21] Hence the apparent variability of D is probably a reason for the shape of the desorption curve. But then it remains unexplained why the sorption behavior resembles curve B more than curve A. The proposed existence of tightly bound water molecules (or their reaction products) can explain why desorption at 110° does not come close to reversing the sorption stress change in experimentally accessible periods of time. This tightly bound water might diffuse so much more slowly than the rest that it would be effectively immobile. Higher temperatures would drive off more of this water due to increased diffusivity and also due to increased thermodynamic driving force for de-binding.

It should be possible to extract information about relative diffusivities from desorption stress measurements, but the strategy employed must be different from the one that was used for sorption because of the form of the desorption curves. Another method that can be applied to data following Eq.(2) involves measuring the slope of the curve where stress change is approximately linear with respect to $t^{1/2}$. Let us define this slope as y , i.e.,

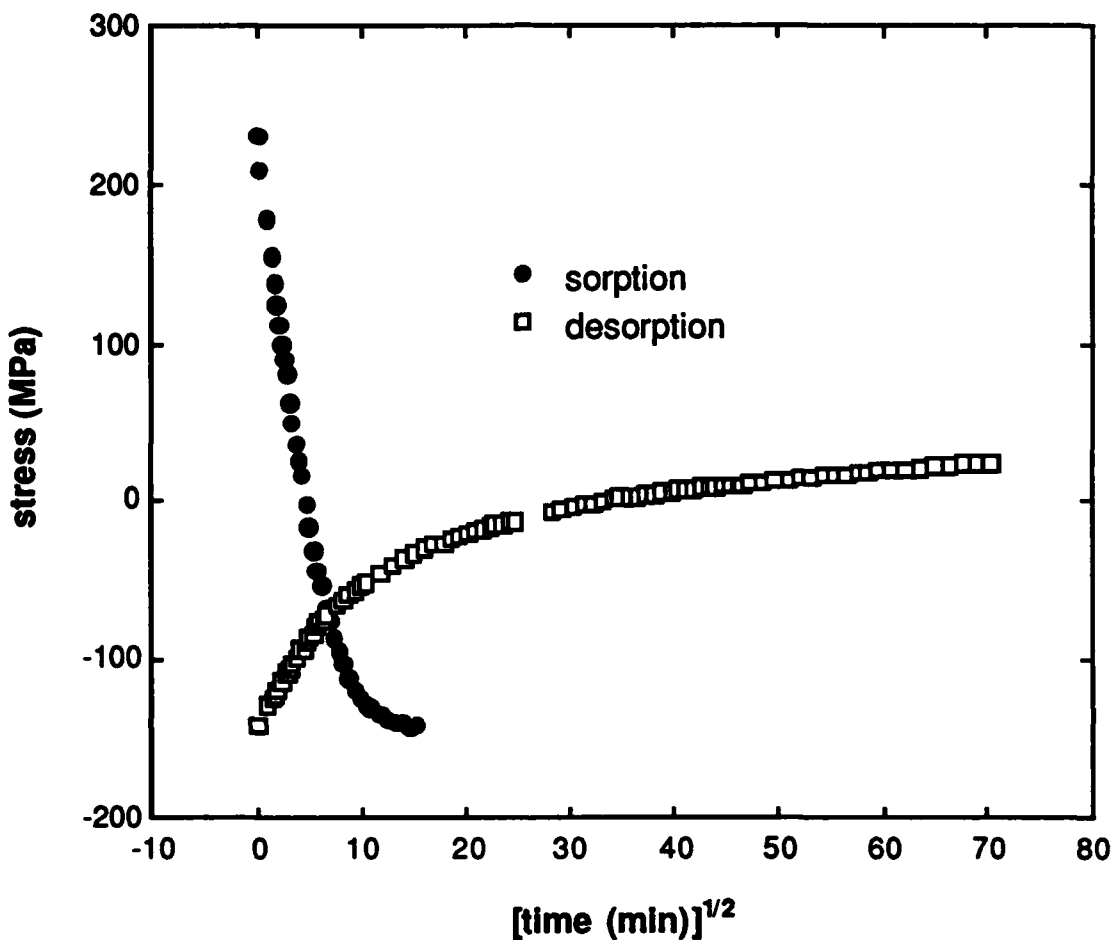


Fig. 6 Desorption behavior compared to sorption behavior of the same film (3 wt% P). $T = 110^\circ\text{C}$.

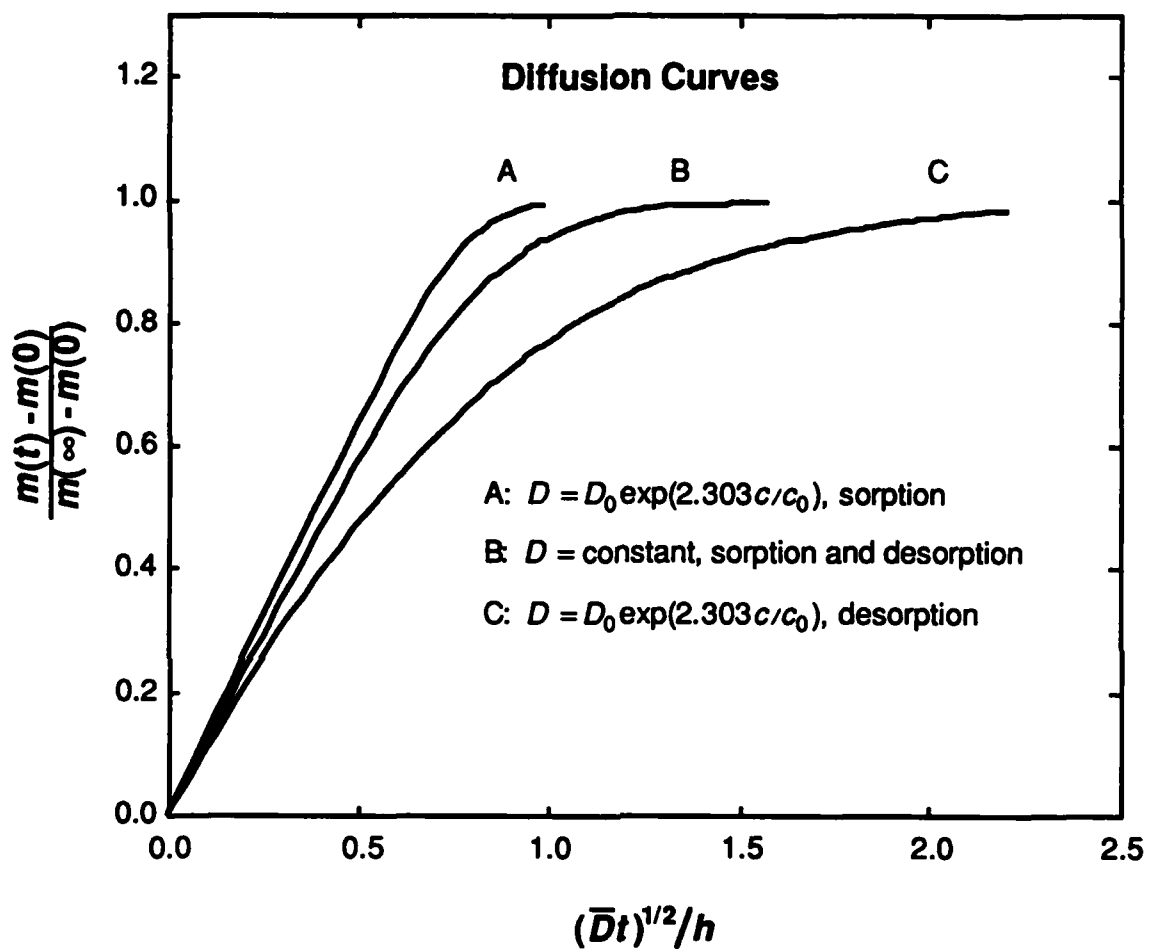


Fig. 7 Curves for diffusion in a sheet in terms of dimensionless parameters for constant and variable- D cases. For sorption, the initial concentration is zero and the saturation concentration is c_0 . For desorption, these states are reversed. \bar{D} is the average diffusion coefficient. Curve B represents Eq. (1).

$$\psi = \left. \frac{d\sigma}{d(t^{1/2})} \right|_{\Delta\sigma \rightarrow 0}. \quad (4)$$

It can also be shown that by Eq. (2), D is related to y by the following relation:

$$D = 0.785 \left(\frac{\psi h}{\Delta\sigma_*} \right)^2. \quad (5)$$

For sorption and desorption involving concentration-dependent diffusivity, such as illustrated in Fig. 7, a similar relation holds, assuming D_s is proportional to D_m :

$$\bar{D} \propto \left(\frac{\psi h}{\Delta\sigma_*} \right)^2. \quad (6)$$

where the constant of proportionality depends on the function $D = f(c)$ and whether the reaction is sorption or desorption. This relation can be used as a basis for a new comparison of the diffusivities of the 430°-annealed samples discussed earlier. Post-saturation desorption data at 110° yielded y values for each film. Assuming the effective D_s was constant for this set of samples, $(yh)^2$ is proportional to \bar{D} by Eq. (6). In Fig. 8, a plot of $(yh)^2$ versus annealing time is superimposed on the plot of Fig. 4, which gives D values based on sorption results. The trends are similar, indicating that $(yh)^2$ is indeed a measure of diffusivity. The annealed-sample points can be made to align quite well, as shown, but then the unannealed-sample points do not coincide. This difference might reflect a real difference in diffusivity, since the unannealed sample used for desorption had not been dried at 300°C like the others. The drying treatment may have had more of an effect than was indicated earlier by sorption tests. In fact, the desorption method may in some cases yield more reliable comparisons of diffusivity than the sorption method. For desorption starting from a saturated state, unlike sorption starting from an incompletely dry state, the initial concentration is uniform and reproducible. However, the effective value of

D_s may not be practically determinable for desorption, so diffusivity comparisons can only be made among conditions for which D_s can be assumed to be constant or can somehow be estimated accurately.

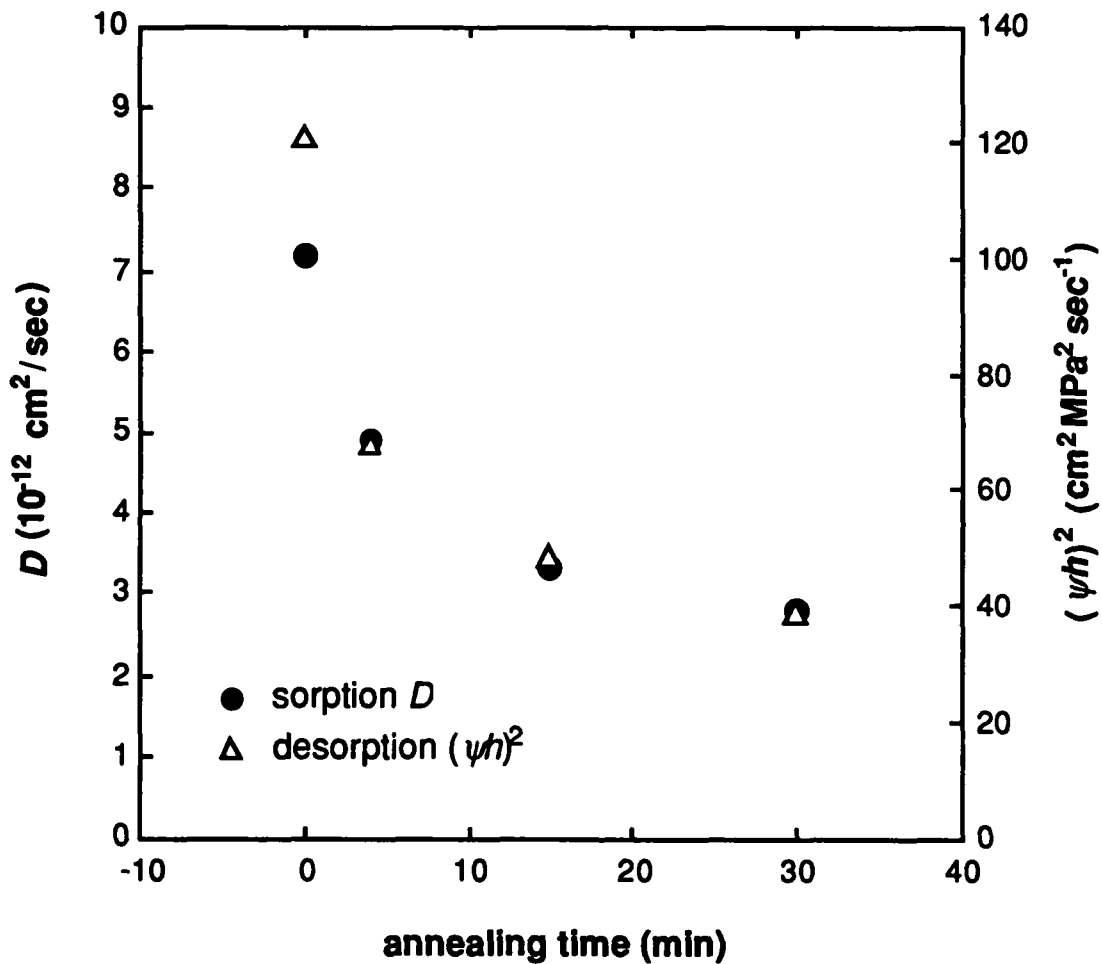


Fig. 8 D calculated from 110°C-sorption data and $(\psi h)^2$ from 110°C-desorption data versus prior annealing time at 430°C for 3-wt%-P films.

6. Summary

A series of experiments was conducted in which stress measurements made on phosphosilicate glass thin films under a variety of conditions were analyzed to yield information about the interaction of the films with water. Deposition rate, deposition temperature, and deposition-furnace residence time were approximately equal for all films, and the films were kept in a dry environment until used. Stress changes occurring during exposure of the films to steam at one atmosphere pressure at various temperatures were analyzed on the basis of a sorption model in which the diffusion coefficient of water was assumed constant and stress changes were assumed proportional to water concentration. The resulting values of D decreased with increasing phosphorus content and yielded activation energies of 0.40–0.45 eV for diffusion. Diffusivity decreased markedly as the result of annealing treatments at the deposition temperature (430°C) and above. Direct measurements of water content by moisture evolution analysis revealed that water concentration changes had a larger effect on stress at low concentrations than they did at higher concentrations, contrary to what had been assumed. However, sorption data re-analyzed in terms of this new information yielded D values that differed by a constant from those calculated originally. Experiments involving sorption in environments in which the partial pressure of water vapor was less than one atmosphere indicated that diffusivity increased with water concentration, again contrary to assumption. Despite flaws in the model used for analysis, the various sorption experiments conducted appear to have yielded valid information about *relative* values of *average* diffusion coefficients. Desorption stress data was shown to have a very different form from sorption data, explainable in part in terms of the concentration dependence of diffusivity. This data was also used successfully to determine diffusivity trends. A qualitative description of PSG and its interaction with water was developed to explain the various experimental observations. In this model,

water is contained in and moves through pores in PSG. The pores and their interconnections have a distribution of sizes, and the average size can be decreased by annealing. "Water" in the film exists in forms having different chemical structures, binding energies, mobilities, and effects on stress. Infrared spectroscopy performed on samples subjected to various treatments confirmed that some of the sorbed water reacts with the glass to form hydroxyl groups in at least two ways and that some forms of moisture can be baked out more easily than others.

7. References

1. W. Kern, "Thin film technology for advanced semiconductors, part 2b-deposited dielectrics for VLSI," *Semiconductor International* 8(7), 121 (1985).
2. *Microelectronic Materials and Processes*, edited by R. A. Levy (Klewer, Dordrecht, Netherlands, 1989), Chap. 6.
3. W. Kern, G. L. Schnable, and A. W. Fisher, "CVD glass films for passivation of silicon devices: preparation, composition, and stress properties," *RCA Review* 37(1), 3 (1976).
4. W. A. Pilskin, "Comparison of dielectric films deposited by various methods," *J. Vac. Sci. Technol.* 14(5), 1064 (1977).
5. Y. Shioya and M. Maeda, "Comparison of phosphosilicate glass films deposited by three different chemical vapor deposition methods," *J. Electrochem. Soc.* 133(9), 1943 (1986).
6. W. Kern and G. Schnable, "Chemically vapor-deposited borophosphosilicate glasses for silicon device applications," *RCA Review* 43(3), 423 (1982).
7. *VLSI Technology*, edited by S. M. Sze (McGraw-Hill, New York, 1983), pp. 629-630.

8. N. Nagasima, H. Suzuki, K. Tanaka, and S. Nishida, "Interaction between phosphosilicate glass films and water," *J. Electrochem. Soc.* **121**(3), 434 (1974).
9. C. R. M. Grovenor, *Microelectronic Materials* (IOP/Hilger, Bristol, U. K., 1989), p. 264.
10. D. Pramanik, "CVD dielectric films for VLSI," *Semiconductor International* **11**(7), 94 (1988).
11. M. Noyori and Y. Nakata, "Interaction between water and scaled CMOS FET's with phosphosilicate glass passivation films," *J. Electrochem. Soc.* **131**(5), 1109 (1984).
12. R. H. Doremus, *Glass Science* (J. Wiley & Sons, New York, 1973).
13. J. A. Aboaf, "Stresses in SiO₂ films obtained from the thermal decomposition of tetraethylorthosilicate – effect of heat treatment and humidity," *J. Electrochem. Soc.* **116**(12), 1732 (1969).
14. H. Sunami, Y. Itoh, and K. Sato, "Stress and thermal expansion coefficient of chemical-vapor-deposited glass films," *J. Appl. Phys.* **41**(13), 5115 (1970).
15. A. Shintani, S. Sugaki, and H. Nakashima, "Temperature dependence of stresses in chemical vapor deposited vitreous films," *J. Appl. Phys.* **51**(8), 4197 (1980).
16. I. Blech and U. Cohen, "Effects of humidity on stress in thin silicon dioxide films," *J. Appl. Phys.* **53**(6), 4202 (1982).
17. W. Kern, "Densification of vapor-deposited phosphosilicate glass films," *RCA Review* **37**(1), 55 (1976).
18. C. H. Amberg and R. McIntosh, "A study of adsorption hysteresis by means of length changes of a rod of porous glass," *Can. J. Chem.* **30**, 1012 (1952).
19. D. H. Bangham, "The Gibbs adsorption equation and adsorption on solids," *Trans. Faraday Soc.* **33**, 805 (1937).
20. L. W. Winkle and C. W. Nelson, "Improved atmospheric-pressure chemical-vapor-deposition system for depositing silica and phosphosilicate glass thin films," *Sol. State Tech.* **24**(10), 123 (1981).

21. J. Crank, *Mathematics of Diffusion*, 2nd edition (Clarendon, Oxford, 1975).
22. E. J. McInerney and P. A. Flinn, "Diffusivity of moisture in thin films," *Annu. Proc. Reliab. Phys. [Symp.]*, 20th, (1982), pp. 264-267.
23. R. M. Levin, "Water adsorption and densification of phosphosilicate glass films," *J. Electrochem. Soc.* **129**(8), 1765 (1982).
24. *VLSI Technology*, edited by S. M. Sze (McGraw-Hill, New York, 1983), p. 136.
25. N. Hackerman and A. C. Hall, "The adsorption of water vapor on quartz and calcite," *J. Phys. Chem.* **62**(10), 1212 (1959).
26. K. Nassau, R. A Levy, and D. L. Chadwick, "Modified phosphosilicate glasses for VLSI applications," *J. Electrochem. Soc.* **132**(2), 409 (1985).
27. L. A. Girifalco, *Atomic Migration in Crystals* (Blaisdell, New York, 1964).
28. W. A Pliskin, "Use of infrared spectroscopy for the characterization of dielectric films on silicon," in *Semiconductor Silicon*, edited by H. R. Huff and R. R. Burgess (Electrochemical Society, Princeton, 1973), pp. 506-539.
29. K. Hurley, "Process conditions affecting boron and phosphorus in borophosphosilicate glass films as measured by FTIR spectroscopy," *Solid State Technol.* **30**(3) (1987).

C. A Model of Void Growth in Encapsulated Metal Lines

(A.I. Sauter Graduate Research Assistant)

1. Introduction

A model has been developed to predict void growth in encapsulated metal lines under stress, based on a grain boundary diffusion mechanism. The model is a synthesis of two others: a simple line model which is valid at long times but breaks down at $t = 0$, and a sphere model which is valid at short times but places unrealistic limits on the void size at long times. The combination model brings together the best elements of each of the other two for a complete description of void growth in an encapsulated line. Void size and time-to-failure data from the literature are compared with the model predictions.

2. Simple Line Model

The Model

As a first approach to the problem of a void growing in an encapsulated line under a hydrostatic tensile stress, consider the case of a void nucleus situated on a grain boundary in an infinitely long metal line (Figure 1). The stress in the line is relieved at the location of the void nucleus, resulting in the establishment of a stress gradient between the void and other points in the line. This in turn results in a vacancy concentration gradient, and thus a chemical potential gradient for vacancies, which causes them to diffuse toward the void. It is assumed that grain boundary diffusion dominates, and lattice diffusion is neglected. Because of symmetry, we consider only the right half of the line. In the steady state, the flux of vacancies in the grain boundaries can be written:

$$J_v = - \frac{2\delta D_{gb}}{dkT} \frac{d\sigma}{dx}. \quad (1)$$

where D_{gb} is the grain boundary diffusion coefficient, δ is the grain boundary thickness, d is the grain diameter, and kT has its usual meaning.

Any spatial variation in the vacancy flux at a point in the line results in the accumulation (or depletion) of matter at that point. We imagine that the line is rigidly passivated, so that the

addition of matter at any point in the line relieves the hydrostatic stress. Therefore the rate of mass accumulation is related to the stress relaxation rate in the following way:

$$\frac{d\sigma}{dt} = -B\Omega \frac{dJ_v}{dx}, \quad (2)$$

where B is the bulk modulus of the line, and Ω is the atomic volume of aluminum.

Differentiating (1) and substituting into the previous expression results in a Fick's-Second-Law-type governing equation:

$$\frac{d\sigma}{dt} = \frac{2\delta D_{gb}}{dkT} B\Omega \frac{d^2\sigma}{dx^2}. \quad (3)$$

With the initial and boundary conditions $\sigma(0, t) = 0$, and $\sigma(\infty, t) = \sigma(x, 0) = \sigma_0$, the solution to this equation is the familiar error function:

$$\sigma = \sigma_0 \operatorname{erf}\left(\frac{x}{2\sqrt{Kt}}\right), \quad (4)$$

where $K = \frac{2B\Omega\delta D_{gb}}{dkT}$.

The rate of void growth at any time is related to the vacancy flux at $x = 0$ thus:

$$\frac{dV}{dt} = -2J_v(\pi R^2)\Omega, \quad (5)$$

with the factor of two coming in because we now consider diffusion from both halves of the line. Substituting for J_v (1), differentiating σ with respect to x and evaluating at $x = 0$, we have

$$\frac{dV}{dt} = \frac{4\pi R^2 \Omega \delta D_{gb}}{dkT} \frac{\sigma_0}{\sqrt{\pi Kt}}. \quad (6)$$

Equation (6) may be integrated to obtain the void volume as a function of time.

Model Predictions

In order to graphically depict the results of the model, the following parameters are used:

$$\sigma_0 = 600 \text{ MPa}$$

$$x = R = 1 \mu\text{m}$$

$$\delta D_{gb} = 5 \times 10^{-14} \exp\left(-\frac{84,000}{8.31 * T}\right)^l$$

$$B = 79 \text{ GPa}$$

$$\Omega = 1.66 \times 10^{-29} \text{ m}^3 \text{ s}^2$$

$$k = 1.38 \times 10^{-23} \text{ J / mole K}^3$$

where δD_{gb} , B and Ω are properties of aluminum.

Figure 2 shows the volume growth rate of the void as a function of time. This figure clearly shows the main difficulty of this model, namely that the growth rate has a singularity at $t = 0$. Thus, while the growth rates at longer times may be reasonable, at short times this model is unrealistic. This singularity means also that the model overpredicts void size and stress relaxation, since the model overpredicts the amount of void growth that occurs initially. The growth rate at longer times varies by about a factor of 50 for a grain size variation of an order of magnitude.

While this model may be useful for predicting long time growth rates, the singularity in the growth rate at $t = 0$ makes short time predictions unreasonable. In addition, the void size and stress relaxation are overpredicted for all times due to the initially infinite growth rate. The singularity arises because the boundary condition $\sigma(0, t) = 0$ is incompatible with the initial condition $\sigma(x, 0) = \sigma_0$. These two conditions result in an initially infinite stress gradient at $x=0$. In order for this to be a useful formulation of the problem, a boundary condition that does not induce singular behavior is needed.

In the next section we consider a model for the behavior of a void in an encapsulated line under stress at short times, with the idea that the stress profile resulting from such a model can be used as a boundary condition to remove the singularity from this calculation.

3. Void Growth at Short Times

The Model

In order to model the initial stages of the growth of a void in a body under hydrostatic stress, we consider a sphere of material with a small void nucleus at its center. Figure 3 shows such a sphere. In (a), the sphere is stress free at temperature T_0 . If the outer

boundary ($r = R$) is fixed and the temperature is lowered to $T < T_0$, a hydrostatic tension stress, σ_0 , develops in the sphere (b). This stress tends to cause the void to grow. Imagine that the sphere is first released from its constraint (c), and then the void grows. This results in a displacement of the outer dimensions of the sphere if the body behaves incompressibly (d). If the sphere is then elastically stretched to fit its constraint, the stress required to be applied to the sphere is smaller than σ_0 (e). Thus the growth of the void reduces the hydrostatic stress.

We initially assume that this material is incompressible, so that the volume of material is unchangeable. Then a simple viscous flow law for the sphere can be written as

$$d\sigma_{rr} = 2\eta \dot{a} a^2 \frac{dr}{r^4}, \quad (7)$$

where η is the viscosity, a the current void size, and \dot{a} the current void growth rate.

Integrating, subject to the condition that the surface of the void is traction free (i.e.

$\sigma_{rr}(r=a)=0$), and evaluating at $r = R \gg a$, we find

$$\sigma_{rr}(R) = \frac{2\eta}{3} \frac{\dot{a}}{a}. \quad (8)$$

Equation (9) provides the relationship between the far field stress and the void growth rate for a given void size.

If we now imagine that the outer boundary of the sphere is rigidly fixed at R , then the growth of the hole must be elastically accommodated by the body. Thus

$$\frac{dV}{dt}_{\text{sphere}} = 0 = \frac{dV}{dt}_{\text{elastic}} + \frac{dV}{dt}_{\text{void}}, \quad (9)$$

i.e. the total volume change must be zero, so hole growth results in elastic compression of the sphere. Since the first term on the right hand side of equation (9) is related to the stress, and the second term is related to the void size, we have

$$\frac{d\sigma}{dt} = - \frac{3B\dot{a}a^2}{R^3}. \quad (10)$$

Differentiating Equation (8) gives

$$\frac{d\sigma}{dt} = \frac{2\eta}{3} \frac{d}{dt} \left(\frac{\dot{a}}{a} \right). \quad (11)$$

Recognizing that $\dot{a}^2 = \frac{1}{3} \frac{d}{dt} a^3$, equations (10) and (11) can be solved simultaneously to give expressions for void size and stress as functions of time:

$$a^3 = a_0^3 \left[\frac{\sigma_0 + B \left(\frac{a_0}{R} \right)^3}{\sigma_0 \exp \left(-\frac{9}{2\eta} \left(\sigma_0 + B \left(\frac{a_0}{R} \right)^3 \right) t \right) + B \left(\frac{a_0}{R} \right)^3} \right], \quad (12)$$

(equation (12) is simply converted to void volume through multiplying by $4\pi/3$)

and

$$\sigma = \sigma_0 - B \left(\frac{a_0}{R} \right)^3 \left[\frac{\sigma_0 + B \left(\frac{a_0}{R} \right)^3}{\sigma_0 \exp \left(-\frac{9}{2\eta} \left(\sigma_0 + B \left(\frac{a_0}{R} \right)^3 \right) t \right) + B \left(\frac{a_0}{R} \right)^3} - 1 \right]. \quad (13)$$

We now define

$$\eta = \frac{d^3 k T}{42 \pi \Omega \delta D_{gb}}, \quad (14)$$

in order to incorporate a grain boundary diffusion mechanism into this model. The right hand side of equation 14 is from a diffusional creep equation given by Frost and Ashby⁴.

Model Predictions

The values of the parameters used in the line model also apply here. Note that the distance used in calculating the stresses in the line model is the same as the radius of the sphere in this model.

Figure 4 shows the void volume as a function of time, for $d = 0.25 \mu\text{m}$ and various initial void sizes. This plot illustrates the main difficulty with the sphere model, that void growth is limited due to the limited volume of material.

In the line model, when the stress at R is fully relaxed there is still a driving force for the void to continue to grow, since there is still a hydrostatic stress farther down the line. In the sphere model, when the stress at R is relaxed, the void stops growing. The limit on void size is given by the limit of V as $t \rightarrow \infty$:

$$V = V_0 + \frac{4}{3} \pi R^3 \frac{\sigma_0}{B}. \quad (15)$$

This corresponds to $3.6 \times 10^{-20} \text{ m}^3$ for $a_0 = 100 \text{ nm}$, as can be seen in Figure 4. This is merely 0.7% of the volume of the sphere. Unless the grain structure in a line is such that continuous grain boundary paths are blocked every linewidth (i.e. a bamboo structure), the void would continue to grow after the stress at R was relaxed by draining vacancies from farther along the line. Thus if the line has long continuous grain boundary paths, the sphere model is not valid.

The sphere solution is useful for predicting short time behavior, but in general, a void in a line would be able to grow larger than the sphere model predicts. The line model, on the other hand, is valid at long times but breaks down at $t = 0$. Thus we now use the stress profile predicted by the sphere solution as a boundary condition in the line model, in an effort to avoid these problems.

Since the stress vs. time at R relation is somewhat complicated, for the purposes of the boundary condition we will approximate it with a simple exponential, thus:

$$\sigma = \sigma_0 \exp\left(-\frac{9}{2\eta}\left(\sigma_0 + B\left(\frac{a_0}{R}\right)^3\right)t\right). \quad (16)$$

We define the coefficient of t in the exponential as A. Using this stress will greatly simplify the task of combining the sphere and line models. It was found that using this simplified stress profile did not introduce any significant error into the model.

4. The Combination Model

Derivation of the Model

In this case we envision an infinitely long cylinder of passivated material, with a void nucleus located at $x = r = 0$ (Figure 5). The radius of the cylinder is R. At $x = R$, the stress is given by equation (16), and the far field stress is σ_0 . This is the same geometry as the

line model, but the boundary condition at $x = R$ is from the sphere model. This removes the singularity arising from the boundary condition in the line model, at the same time avoiding the limited growth problem with the sphere model. At zero time, the stress is everywhere σ_0 , and the governing equation is the same as in the line model, i.e.

$$\frac{d\sigma}{dt} = K \frac{d^2\sigma}{dx^2}, \quad (7.56)$$

where $K = \frac{2B\Omega\delta D_{gb}}{dkT}$. As in the line model, the assumption is made that a continuous grain boundary path exists in the cylinder, and that the void nucleus is located on a grain boundary. This problem is solved using Laplace Transforms⁵. Unfortunately, the expression for the stress cannot easily be deconvoluted, but we nevertheless can obtain an expression for the void growth rate since this depends on the gradient of the stress:

$$\frac{du(R,t)}{dx} = \frac{2\sigma_0 A}{\sqrt{\pi AK}} \exp(-At) \int_0^{\sqrt{At}} \exp(\lambda^2) d\lambda. \quad (17)$$

Though this is not easily solved, the expression $\exp(-At) \int_0^{\sqrt{At}} \exp(\lambda^2) d\lambda$ is known as Dawson's integral, and has been tabulated⁶. Thus it is possible to evaluate equation (17), and obtain the stress gradient at R as a function of time.

The void growth rate is obtained analogously from the line model:

$$\frac{dV}{dt} = \frac{4\pi R^2 \Omega \delta D_{gb}}{dkT} \frac{\sigma_0 \sqrt{A}}{\sqrt{\pi K}} \left[\exp(-At) \int_0^{\sqrt{At}} \exp(\lambda^2) d\lambda \right]. \quad (18)$$

This void growth rate becomes valid at times when vacancies are being drained from places in the line past $x = R$. The growth rate for the combination solution is zero at time zero because there is no contribution to void growth from that far along the line initially. As the void grows, vacancies begin to drain from farther along the line, and the flux at R increases, so the combination model growth rate increases. Eventually, the growth is dominated by diffusion along the line. At long times the combination solution approaches the simple line solution. This means that the exponential boundary condition removes the singularity, but that long time behavior is essentially unchanged.

In order to describe the void growth rate at all times, the following procedure is used. At time zero the initial void growth rate is taken to be that of the sphere solution, i.e.

$$\frac{dV(t=0)}{dt} = \frac{6\pi\sigma_0 a_0^3}{\eta}. \quad (19)$$

The combination solution is assumed to be accurate as soon as it is (a) falling monotonically with time, and (b) smaller than the initial void growth rate. A polynomial fit to the initial part of the combination solution and the growth rate at $t=0$ describes the growth rate at intervening times. An example of this is shown in Figure 6. In this way the short time behavior of the sphere model and the long time behavior of the simple line model are unified to form a complete description of void growth with time.

Model Predictions

One of the most important quantities that the void growth model should be able to predict is failure time. This is calculated first by fitting the log (growth rate) vs. time curve with piecewise polynomials (Figure 6). The result is then numerically integrated.

The time to failure is defined as the time to reach a certain volume. We will choose the failure volume to be such that $a = R/2$, i.e. $V_f = 5.236 \times 10^{-19} \text{ m}^3$ for $R = 1 \mu\text{m}$. Thus a quarter of the cross sectional area of the line has been taken up by a void. While a void of this size would not short circuit a line on its own, it could certainly be troublesome when combined with electromigration.

Failure times have been calculated for a variety of temperatures, grain sizes, and deposition temperatures, using $a_0 = 50 \text{ nm}$. In these calculations, we use $\sigma = 0.26(3B\Delta\alpha\Delta T)$, a relationship predicted by finite element calculations.

In Figure 7, the log of the failure times for a deposition temperature of 500°C versus temperature has been plotted. We would like to be able to describe the dependence of the failure time on temperature and grain size in a simple way, in order to make predictions for cases other than those calculated. The lines through the calculated points in Figure 7 are an equation of the form

$$\log t_f = A + B \log(d) + C \log(\Delta T) + \frac{D}{T}. \quad (20)$$

The best fits to the data are found when $A = 7$, $B = 1$, $C = -2$, and $D = 4226$.

Equation (20) can be written

$$t_f = 10^7 d \Delta T^{-2} \exp\left(\frac{2.303 * 4226}{T}\right). \quad (21)$$

In this form, it can be seen that D is an activation energy. Rewriting $2.303 * 4226$ as Q/R, we find that $Q = 80.9$ kJ/mole. This is very close to the activation energy for grain boundary diffusion that was used to calculate the failure times, i.e. 84 kJ/mole.

ΔT can be written as $\sigma/0.26 * 3B\Delta\alpha$. Then we can write the time to failure as a function only of stress, temperature, and grain size:

$$\frac{t_f \sigma^2}{d} = 10^{19.2} \exp\left(\frac{80,900}{RT}\right). \quad (22)$$

Figure 8 shows the simple Arrhenius relationship of the quantity $\frac{t_f \sigma^2}{d}$ for all of the cases calculated.

Comparisons to Data

Data of Smith et. al⁷

Smith and others⁷ used a thermal wave technique to image voids as they grew at elevated temperatures in encapsulated lines. They reported void size vs. time data for two specimens held at 400°C. They did not report the passivation material, thickness, or deposition temperature, but gave line aspect ratios of 2.0 and 2.8. The lines were aluminum-1%silicon, and they reported a very small grain size, i.e. 0.05 microns. If we assume a stress of 125 MPa in the w/h = 2.0 line and a stress of 94 MPa in the w/h = 2.8 line, we can predict the void size vs. time data quite well. Those stresses correspond to a deposition temperature of about 500°C

Figure 9 compares Smith's data with the predictions of the model. The agreement is good for w/h = 2.8. In the w/h = 2.0 case, the data are very scattered so the model does better at longer times than initially. Smith used the model of Yost⁸ to describe his data. The fits look similar to this model, but the Yost model uses the activation energy as a fitting parameter. This makes it quite simple to fit to data, but it is difficult to determine the mechanism. The best fits to Smith's data for the Yost model give about the activation energy for grain

boundary diffusion in the case $w/h = 2.8$, but in the narrower line the activation energy found is 25% larger than that for grain boundary diffusion in aluminum. This model is superior because we can predict the void size with one mechanism for both cases.

Data of MacPherson and Dunn⁹

MacPherson and Dunn⁹ subjected a number of samples to aging tests between 100°C and 200°C, periodically testing them for failure. The samples were aluminum-1%silicon lines with grain sizes " < 1.2 microns," 3-6 microns wide and passivated with silicon nitride at an unknown temperature. They reported normalized creep rate vs. aging temperature, the former being defined as the inverse of the time to 20% failure divided by the maximum of this quantity in the temperature range.

Figure 10 shows the data of MacPherson and Dunn compared to the model. We assume a grain size of one micron, and a deposition temperature of 210°C. The location of the peak in creep rate is accurately predicted, but the width of the peak is apparently narrower than that measured. However, given the scatter in the two points at 150°C, it is possible that the peak should be narrow as predicted.

The only way to widen the peak is to lower the activation energy. MacPherson and Dunn used their model to describe their data. They used an activation energy 25% lower than that of grain boundary diffusion in aluminum and were able to predict the width of the peak.

Given the scatter in the data, this model does a good job of predicting failure of these samples.

5. Conclusions

A simple model of void growth in an encapsulated line based on grain boundary diffusion of vacancies along the line is valid at long times, but breaks down at $t = 0$. A model of void growth in an encapsulated sphere gives the correct behavior at short times, but is not accurate at long times. Combining the two, by using the stress profile of the second as the boundary condition in the first, produces a model valid for all times. The times to failure predicted by this model were found to follow the simple relation

$$\frac{t_f \sigma^2}{d} = 10^{19.2} \exp\left(\frac{80,900}{RT}\right), \quad (23)$$

where the activation energy is about that of grain boundary diffusion.

The model successfully predicts a variety of data from the literature. Authors presenting void growth and failure data need to report the materials, geometry, grain size, and passivation deposition temperature for their samples, so that accurate comparisons to models may be made. The grain boundary diffusion mechanism explains data that were previously modeled with other unexplained activation energies. Since the model can make predictions based on a single mechanism, it is superior to previous models that use the activation energy as a fitting parameter.

6. References

- 1 H.J. Frost and M.F. Ashby, Deformation-Mechanism Maps, Oxford: Pergamon Press, p.15 (1982).
- 2 H.W. King, J. Mat. Sci., **1**, 79 (1966).
- 3 D.E. Roller and R. Blum, Physics: Mechanics, Waves and Thermodynamics, Volume I, San Francisco: Holden-Day, p. 801 (1981).
- 4 H.J. Frost and M.F. Ashby, Deformation-Mechanism Maps, Oxford: Pergamon Press, p.21 (1982).
- 5 Private communication with Prof D.M. Barnett, Stanford University (1990).
- 6 Handbook of Mathematical Functions, ed. M. Abramowitz and I.A. Stegun, National Bureau of Standards, p.319 (1964).
- 7 W.L. Smith, C. Wells, A. Bivas, F.G. Yost, and J.E. Campbell, Proc. 28th Annual IEEE IRPS, p.200 (1990).
- 8 F.G. Yost, Scripta Metall., **23**, 1323 (1989).
- 9 J.W. MacPherson and C.F. Dunn, J. Vac. Sci. Technol. B, **5**, 1321 (1987).

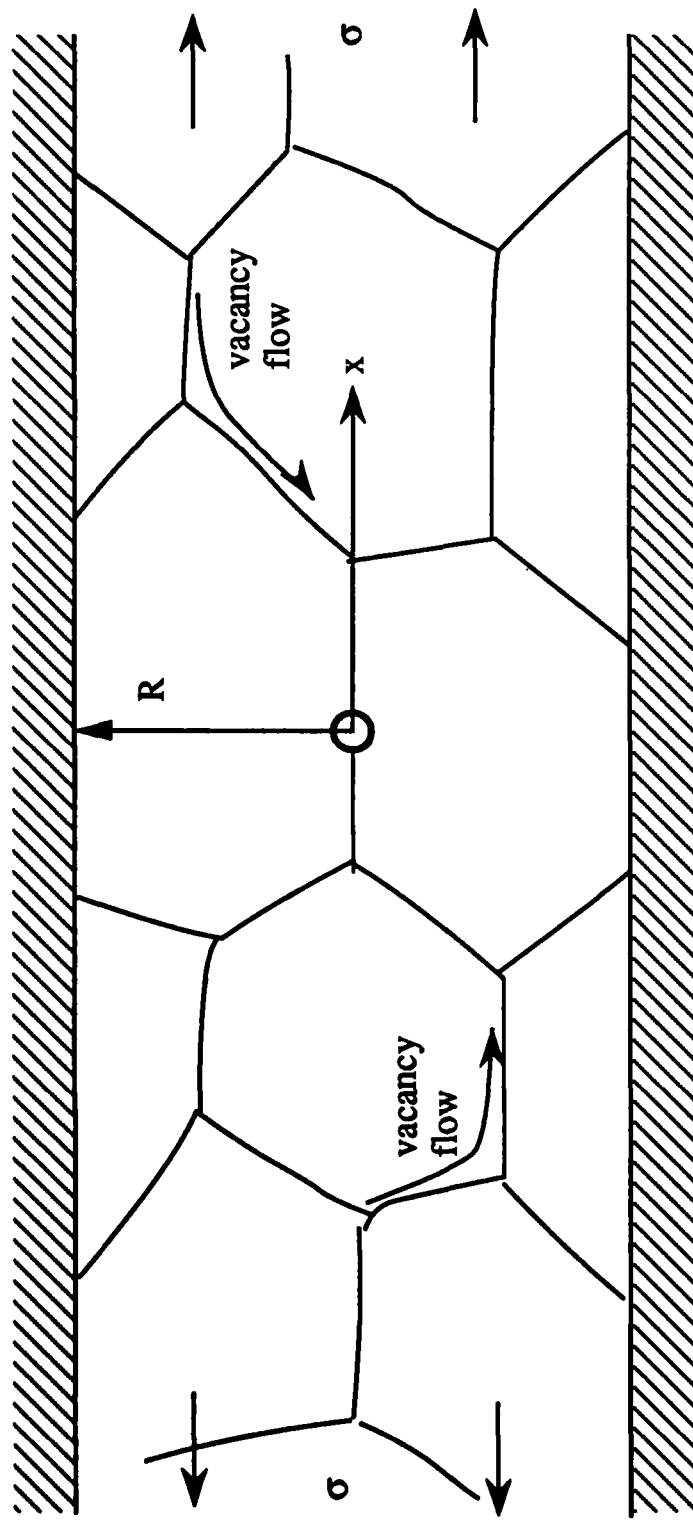


Figure 1. Schematic diagram of the line model. There is a vacancy concentration gradient between the void nucleus and the rest of the line. Therefore vacancies diffuse toward the void, relieving the hydrostatic stress.

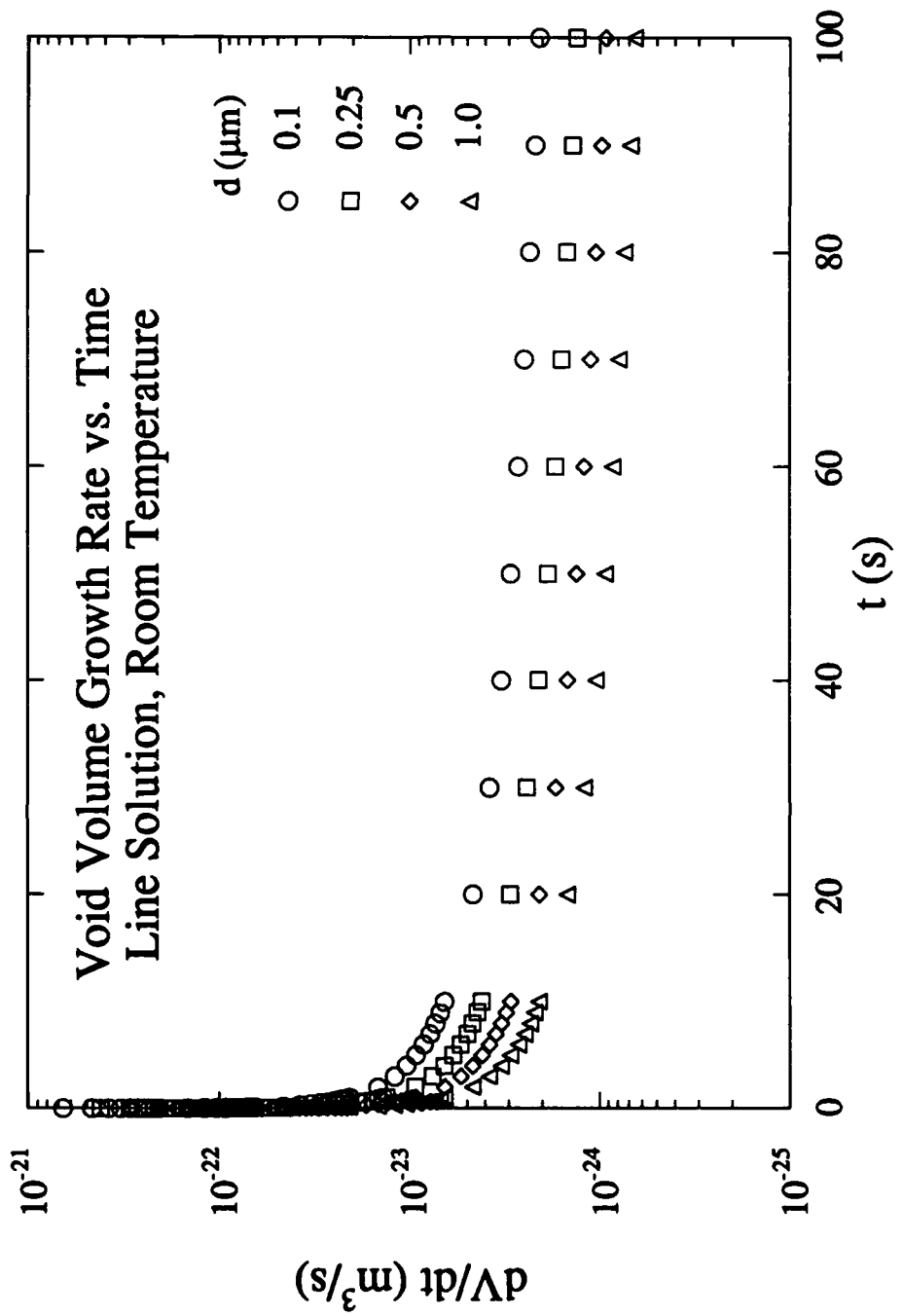


Figure 2. The void growth rate vs. time according to the line model, at $x = R$, for various grain sizes.

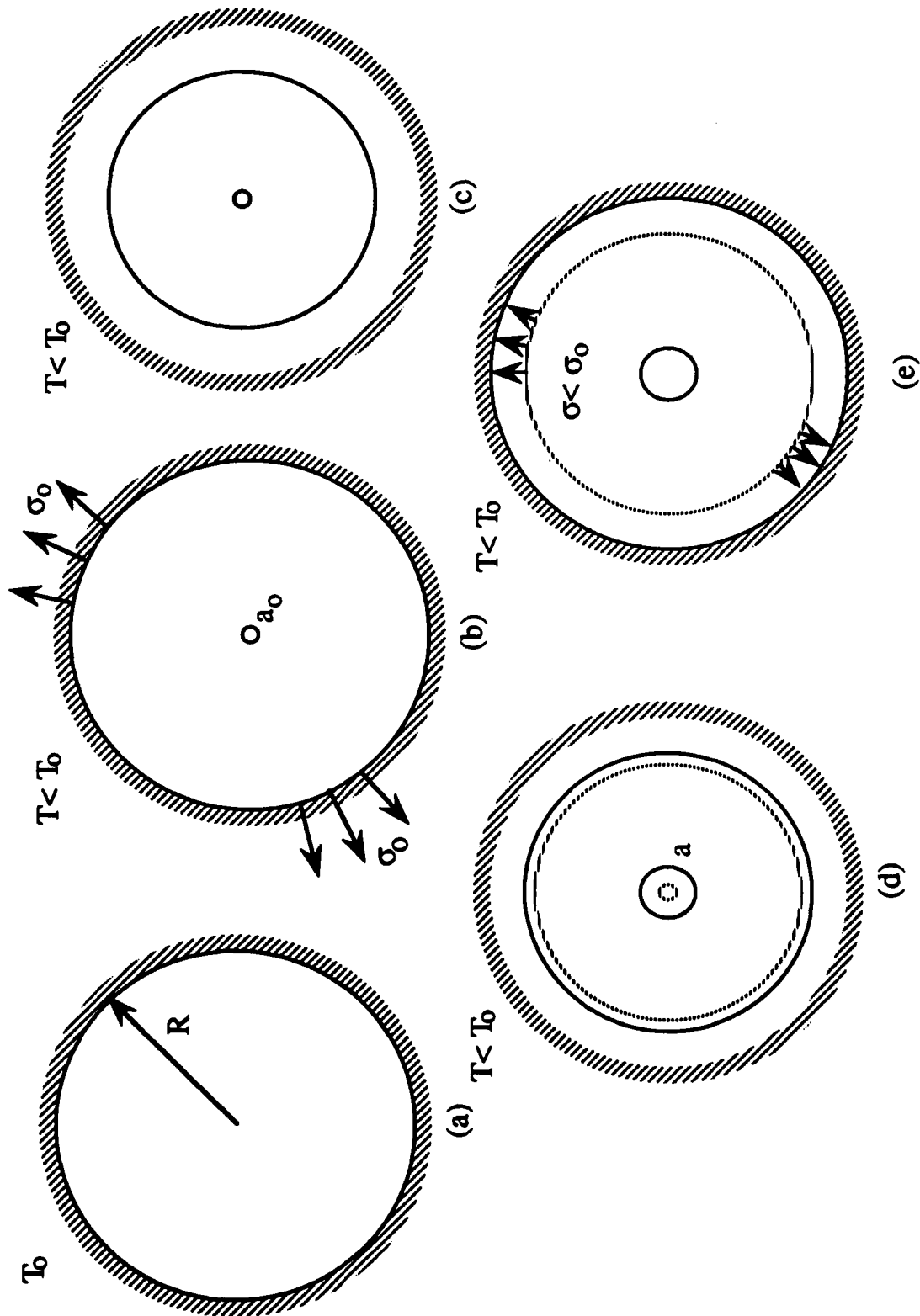


Figure 3. A schematic diagram illustrating the way in which a void growing in a rigidly encapsulated line relieves the hydrostatic stress. (a) Stress-free sphere at T_0 , its outer boundary fixed in space. (b) Temperature lowered to T , producing a hydrostatic stress σ_0 , and a void nucleus of radius a_0 placed at the center of the sphere. (c) Sphere released from its constraint. (d) Void grows, increasing the outer radius of the sphere since the material is incompressible. (e) Stress required to re-attach the sphere to its constraint is smaller than σ_0 .

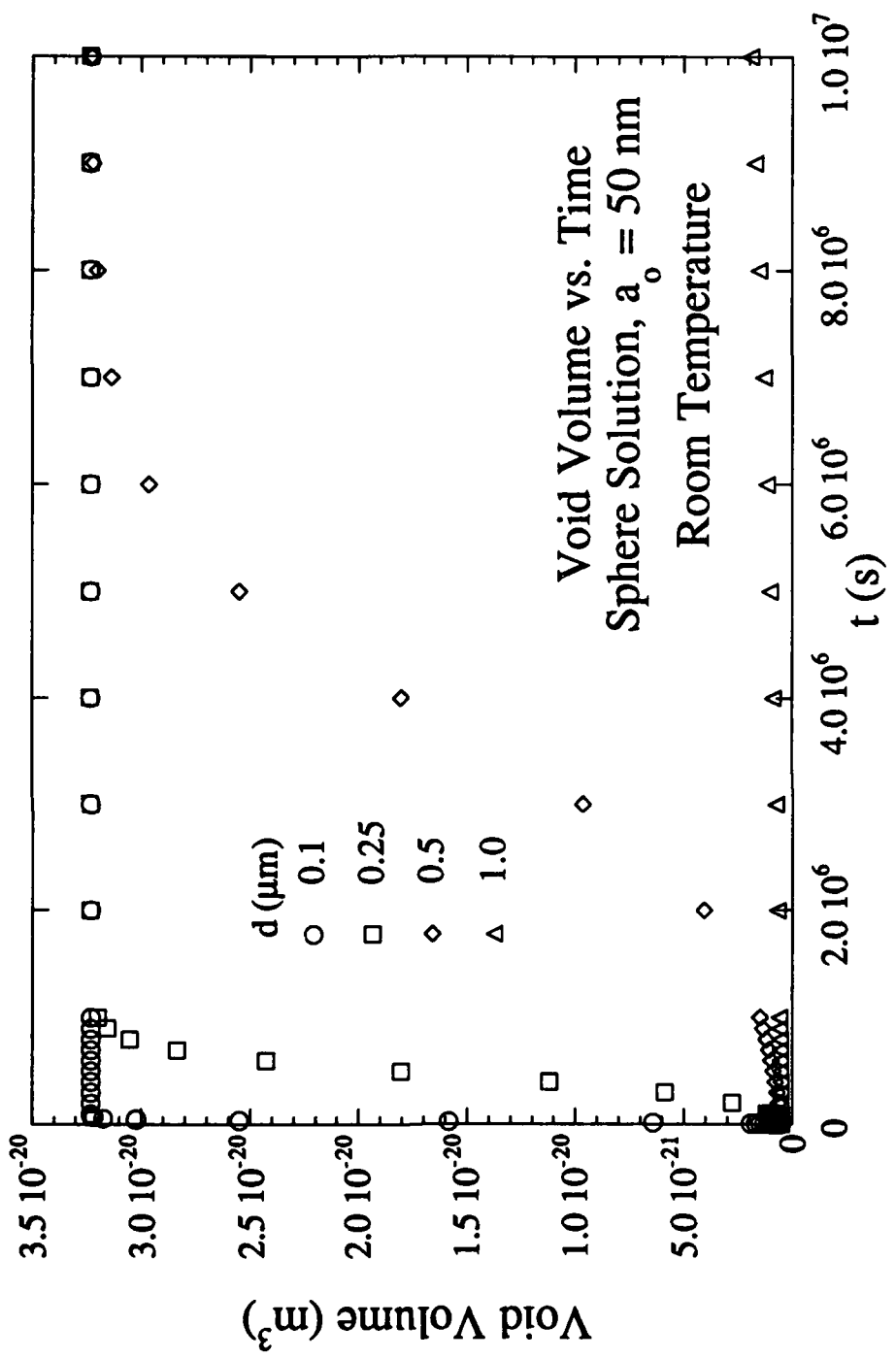


Figure 4. The void volume vs. time according to the sphere model, at $x = R$, $d = 0.25 \mu\text{m}$, for various initial void sizes.

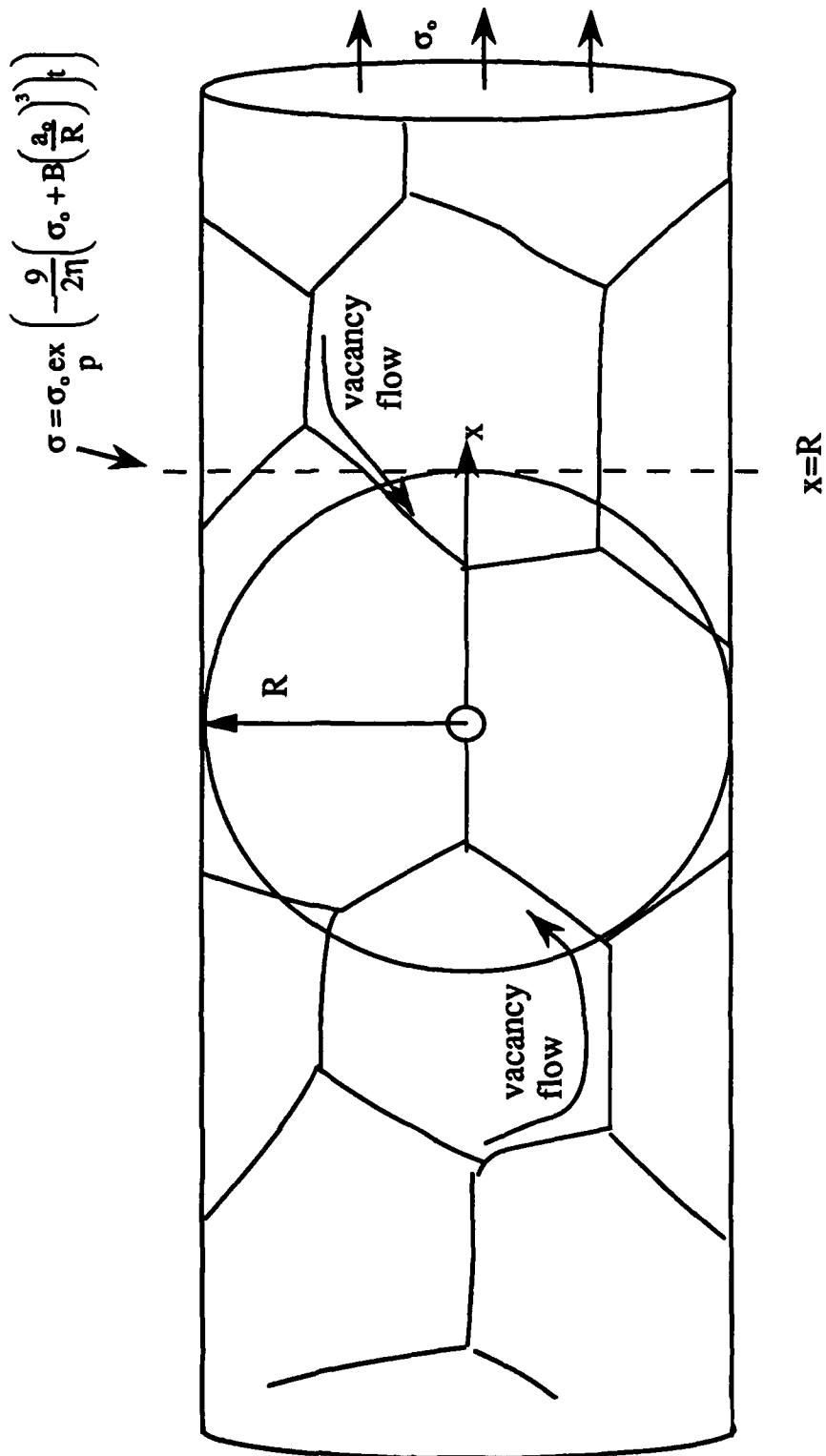


Figure 5. A schematic diagram of the model. The vacancy concentration gradient between the void nucleus and the rest of the line causes vacancies to diffuse toward the void. The stress is assumed to fall exponentially with time at $x = R$.

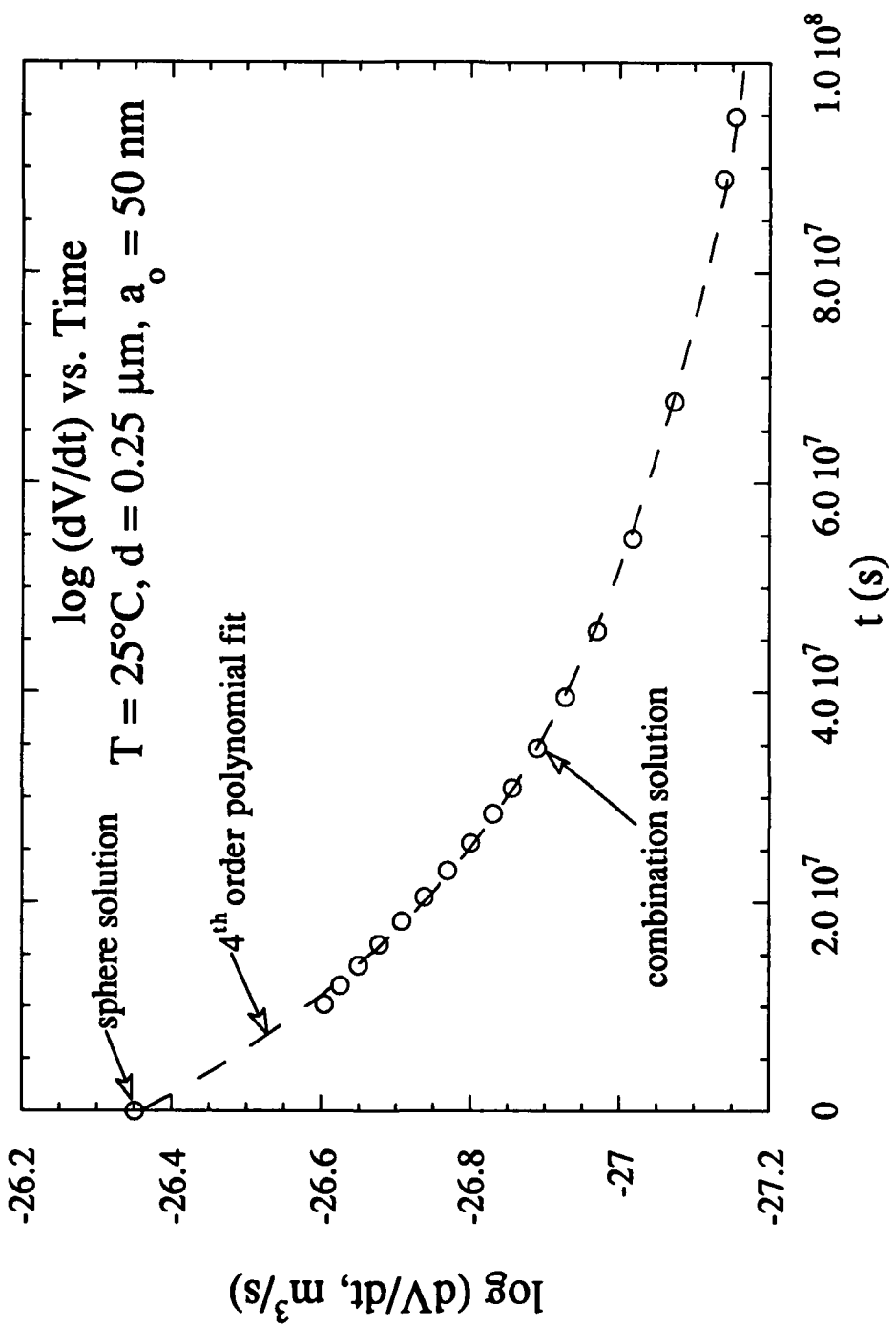


Figure 6. Construction of the void growth rate for the model. The sphere solution is used at $t = 0$ and the combination solution is used at longer times. A polynomial fit between the two gives the growth rate at intermediate times.

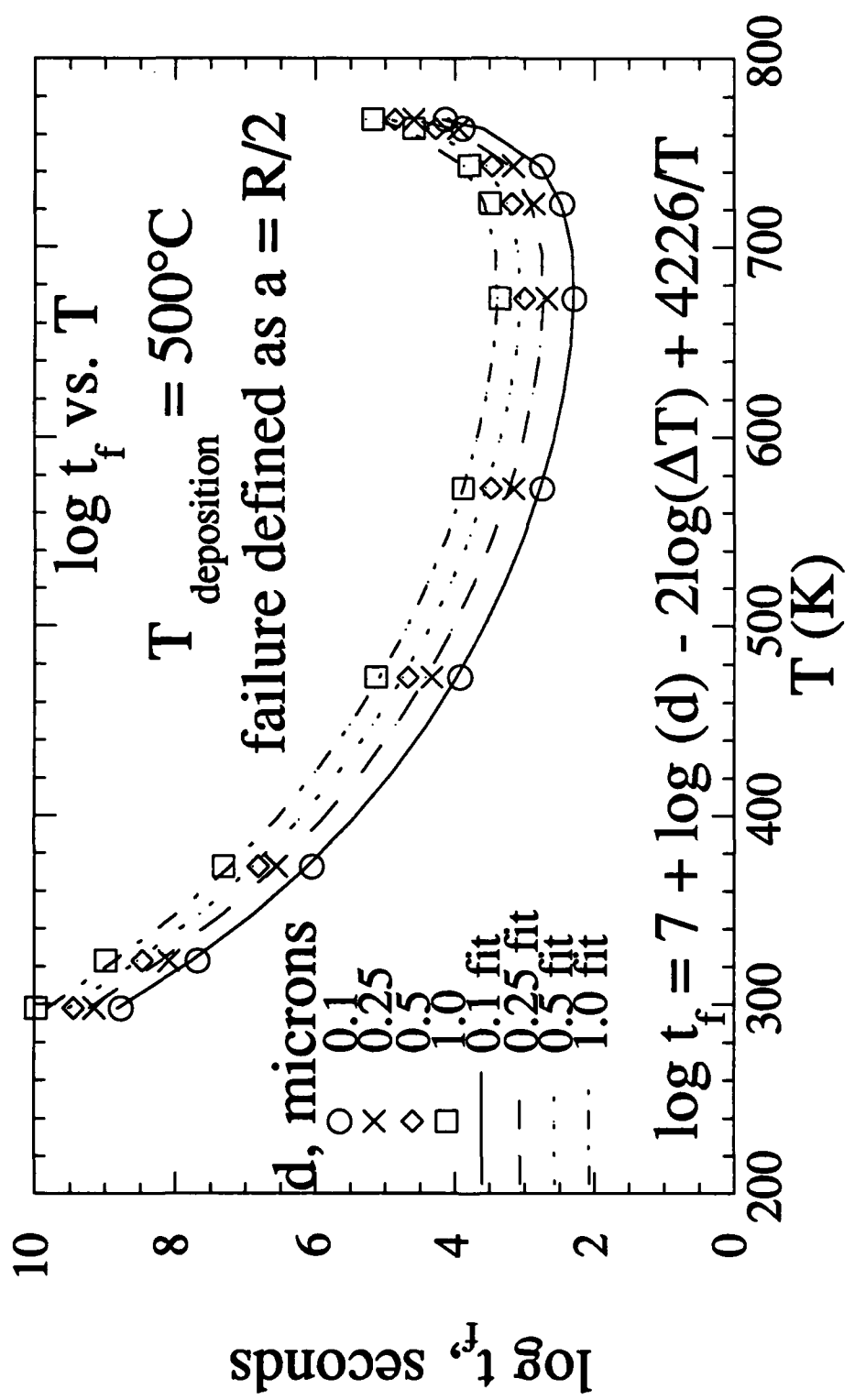


Figure 7 Times to failure vs. temperature for four grain sizes, $a_0 = 50$ nm, and a passivation deposition temperature of 500°C . An equation of the form $\log t_f = A + B\log d + C\log(\Delta T) + D/T$ fits the calculated failure times very well.

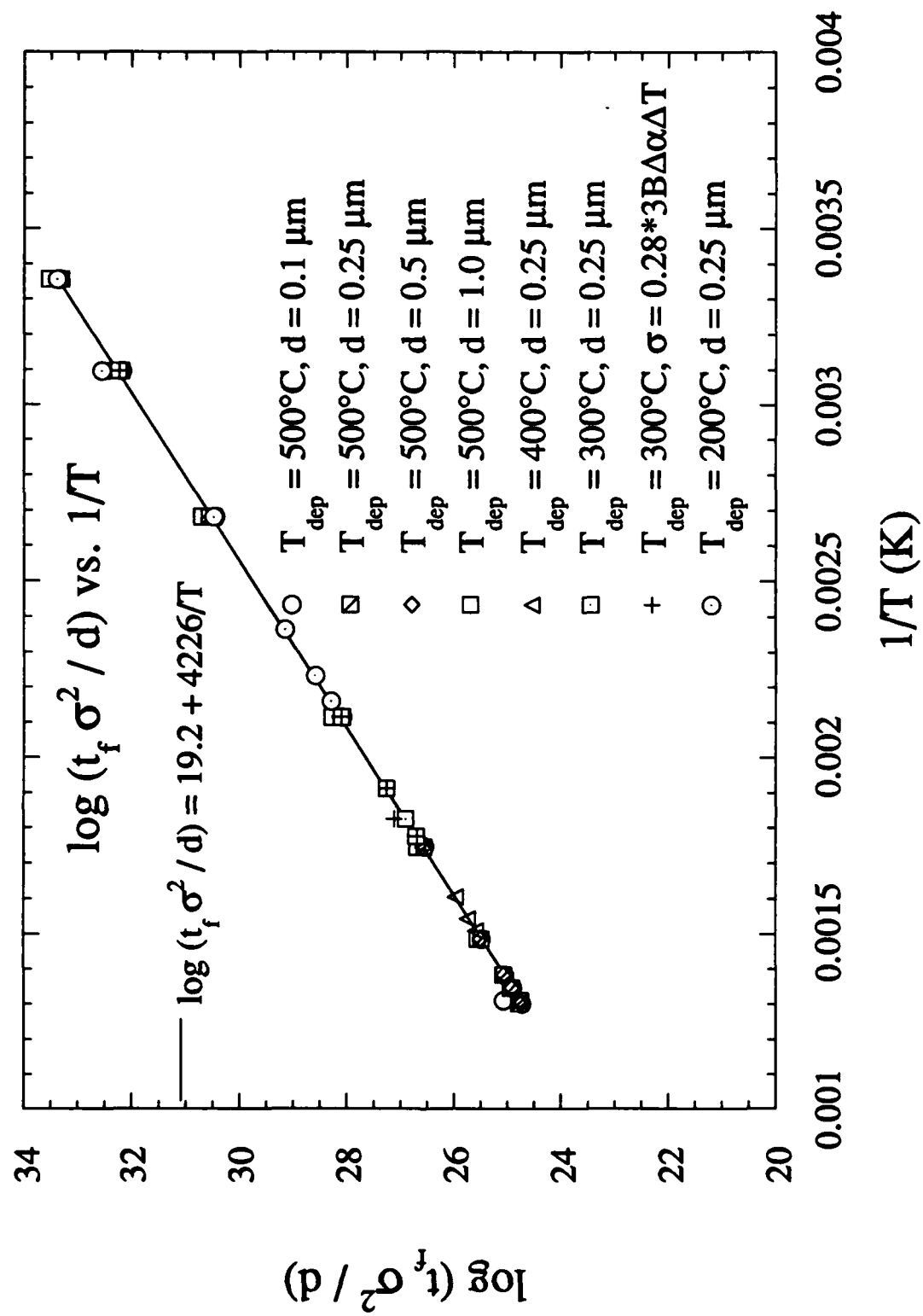


Figure 8. The simple Arrhenius dependence of $t_f^* \sigma^2/d$ on temperature regardless of deposition temperature.

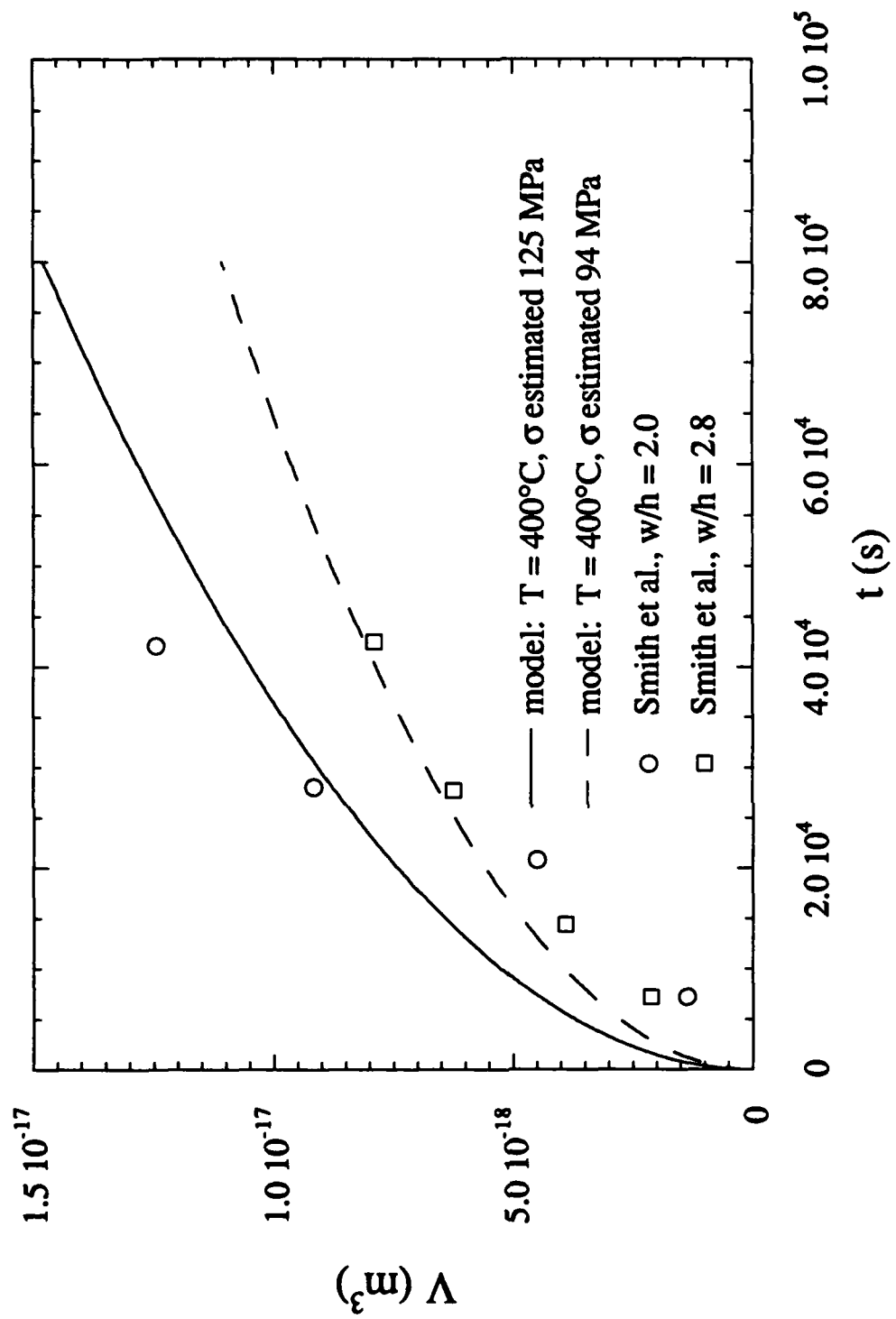


Figure 9. Comparison of the void size data of Smith et al.⁷ with the model. The $w/h = 2.8$ data are well predicted assuming a stress of 94 MPa in the line at 400°C . The data for $w/h = 2$ are more scattered, but the longer time data are predicted by assuming a stress of 125 MPa. Both of these stresses would result from a deposition temperature of about 500°C .

Figure 10. Comparison of the creep rate data of MacPherson and Dunn⁹ with the normalized inverse time-to-failure predictions of the model. The peak in the creep rate is well predicted assuming a deposition temperature of 210°C .

D. The Effect of Oxygen on the Thermal Stability of $\text{Si}_{1-x}\text{Ge}_x$ Strained Layers

D.B. Noble (Graduate Research Assistant)

The purpose of this work is to show experimentally that oxygen in LRP-grown $\text{Si}_{1-x}\text{Ge}_x$ films increases the annealing critical thickness of the layers. We suggest by comparison of these results to those of others studying oxygen in elemental Si and by theoretical modeling that the oxygen in the $\text{Si}_{1-x}\text{Ge}_x$ layers may act as both a solid solution strengthening agent and a dislocation locking atmosphere. The addition of oxygen (and perhaps other elements known to strengthen Si such as nitrogen and phosphorous) to $\text{Si}_{1-x}\text{Ge}_x$ layers provides a method for stabilizing strained films against misfit dislocation formation.

1. Introduction

Thermal Stability

Some of the first annealing experiments performed as part of this work involved a comparison of the thermal stability of LRP layers containing 21% Ge with the thermal stability of MBE layers containing 15% Ge. Figure 1 is a plot of misfit dislocation spacing after annealing as a function of annealing temperature for the LRP and MBE films taken from this work. Misfit dislocation formation is slower in the LRP layers compared to the MBE layers, especially at lower temperatures, despite the larger Ge fraction in the LRP layers. Subsequently, a 15% Ge-LRP film was grown to more closely match the MBE layers in thickness and composition. Misfit dislocations were not found in this layer even after annealing for 4 minutes at 850 °C. A point representing this experiment is also included in Fig. 1. The large difference in thermal stability was attributed to either additional dislocation nucleation sources in the MBE material or additional impediments to dislocation formation in the LRP structures. The results presented in this report show that the major reason for the difference is the high level of oxygen in the LRP films. The effect of oxygen has been demonstrated experimentally and analyzed using standard theories for strengthening mechanisms in crystalline solids. The results in our $\text{Si}_{1-x}\text{Ge}_x$ layers are consistent with the results of Sumino [1], who studied the effect of oxygen in elemental bulk Si, even though Sumino's oxygen levels were at least two orders of magnitude less than those in the $\text{Si}_{1-x}\text{Ge}_x$ films. It has been shown that 15 and 21% Ge LRP films with low oxygen levels are also thermally more stable than the MBE layers mentioned above.

Thus it is likely that a larger number of nucleation sources in the MBE material contributed to the relatively easy dislocation formation kinetics in these films.

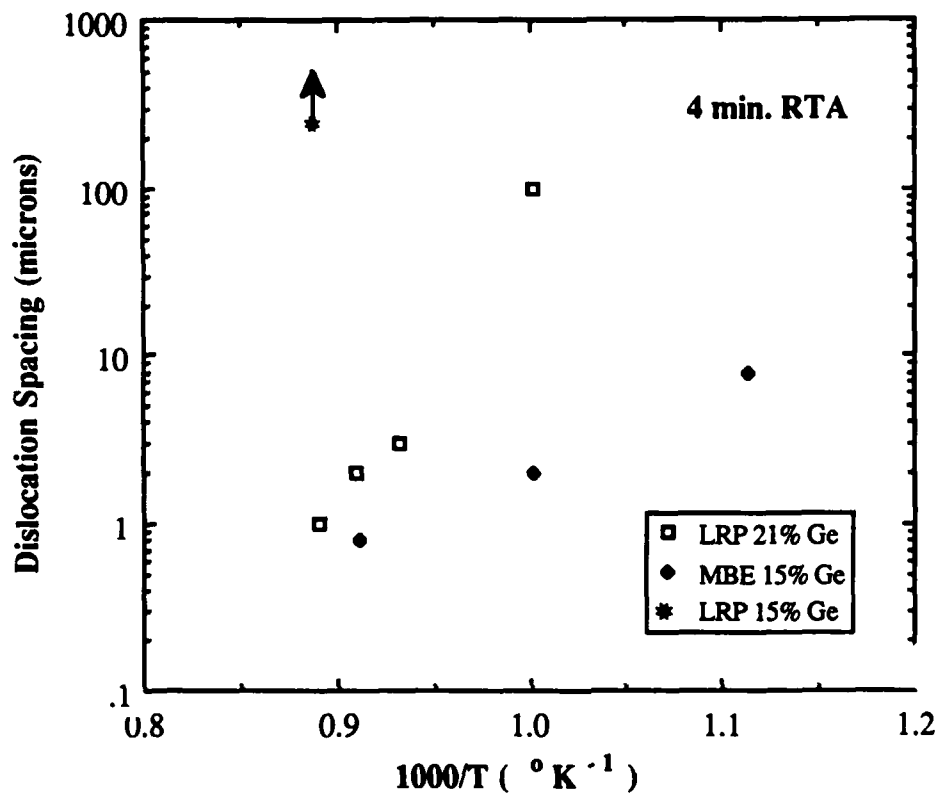


Figure 1 Comparison of mean misfit dislocation spacing in 21% Ge LRP samples and 15% Ge MBE samples (courtesy of K. Wang, UCLA) for 4 minute rapid thermal anneals at several temperatures. One data point for a 15% Ge LRP sample is shown for reference (the arrow means the dislocation spacing was greater than what is indicated by the point).

Oxygen in LRP-grown $\text{Si}_{1-x}\text{Ge}_x$ Films

A brief description of oxygen incorporation into LRP $\text{Si}_{1-x}\text{Ge}_x$ layers is given in this section. More detailed information can be found in Hoyt et al [2]. At a given temperature below about 900 °C oxygen incorporates more readily into $\text{Si}_{1-x}\text{Ge}_x$ layers than into pure Si or pure Ge films. For example, pure Si grown using dichloro-silane (DCS) at a temperature of 700°C contained oxygen at a level below the detection limit of Secondary Ion Mass Spectrometry (SIMS), which is on the order of 10^{17} to 10^{18} cm^{-3} . $\text{Si}_{1-x}\text{Ge}_x$ layers ($0.15 < x < 0.40$), on the other hand, grown under the same nominal conditions, using

DCS and germane, contained as much as two orders of magnitude more oxygen (between 5×10^{19} and $2 \times 10^{20} \text{ cm}^{-3}$). Oxygen was not found in pure Ge layers grown at 625 °C using germane. Thus, there appears to be a cooperative effect between DCS and germane with regards to oxygen incorporation.

In addition to this synergism, there is a growth temperature effect which seems to be active. For fixed partial pressures of reactant gasses the normalized rate of oxygen incorporation into $\text{Si}_{1-x}\text{Ge}_x$ films is approximately constant with increasing temperatures between 625 and about 800°C (a normalized incorporation rate is used here because both Ge fraction and film growth rate change with growth temperature if reactant pressures are held fixed). Films grown at temperatures higher than 800 °C contain only trace amounts of oxygen. The transition between high and low oxygen layers is apparently an abrupt function of temperature which occurs over a temperature range of 50 °C or less. Oxygen free $\text{Si}_{1-x}\text{Ge}_x$ films can be grown in the LRP apparatus at temperatures above 800 °C. Such high temperature growth is undesirable, however, because misfit dislocations form readily at this temperature and growth of high Ge fraction alloys is not possible due to non-planar film growth (islanding). These results point to the importance of understanding the fundamental chemical processes in LRP (CVD) film growth and the importance of controlling impurity levels during film growth

Short of mastering the chemistry of oxygen incorporation during $\text{Si}_{1-x}\text{Ge}_x$ film growth, it is important to produce high purity oxygen free layers grown at low temperatures for use in materials studies and device fabrication. Potential sources of oxygen include water vapor desorbing from the chamber walls, from the quartz wafer holder and from the upstream plumbing and impurities in the source gasses themselves. Of these, the quartz reaction chamber was thought to be the likely major source of oxygen containing species because of its size (large surface area) and proximity to the wafer. The addition to the LRP apparatus of a turbo-pumped manual load-lock chamber which allows wafers to be loaded without exposing this quartz reaction chamber to the ambient was recently completed. The design of the reaction chamber was not changed by the addition of the load-lock. This modification has successfully reduced the background partial pressure of water and oxygen in the system, enabling the growth of high purity $\text{Si}_{1-x}\text{Ge}_x$ layers at low temperatures. Figure 2 compares SIMS data for oxygen in $\text{Si}_{1-x}\text{Ge}_x$ films ($x=0.21$) grown at 625 °C before,(a) and after,(b), the addition of the load-lock chamber. Similar results were obtain for 14.5% Ge layers. Samples used in the SIMS analysis had a Si capping layer to avoid problems associated with the measurement in the near surface region.

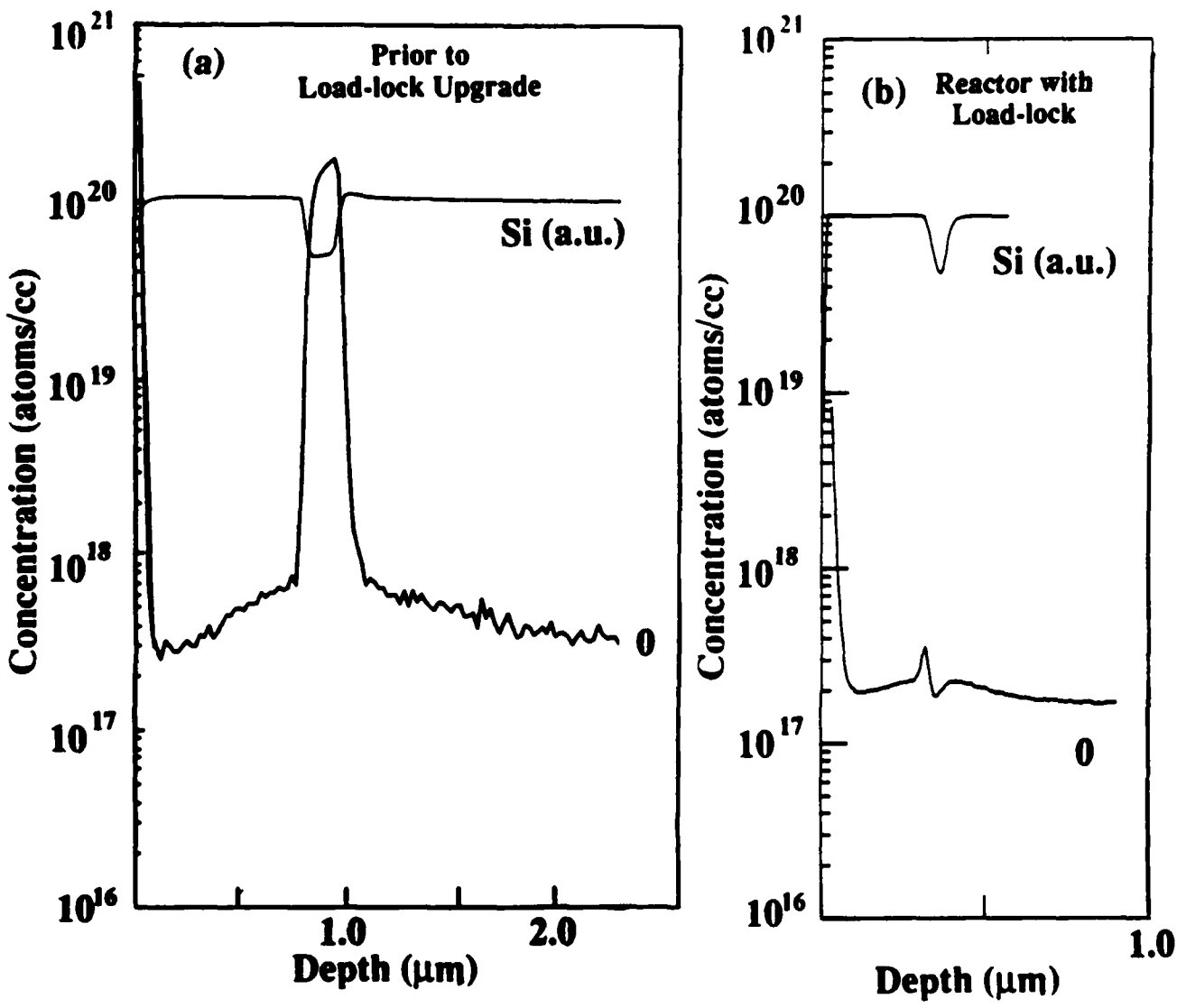


Figure 2 Typical SIMS profiles for $\text{Si}_{1-x}\text{Ge}_x$ ($x=0.21$) layers grown at 625°C (a) before the load-lock (2×10^{20} oxygen atoms/ cm^3 and (b) after the load-lock less than 4×10^{17} oxygen atoms/ cm^3). An interfacial oxygen peak is apparent but the oxygen in the bulk of the $\text{Si}_{1-x}\text{Ge}_x$ is less than the SIMS detection limit.

For the purposes of this work the phrase "high oxygen" describes those $\text{Si}_{1-x}\text{Ge}_x$ layers, both 14.5% and 21% Ge, with oxygen contents of about 10^{20}cm^{-3} grown without the lock-lock. The term "low oxygen" refers to 14.5% Ge films with oxygen contents less than $2 \times 10^{17}\text{ cm}^{-3}$ (SIMS detection limit) and 21% Ge layers with less than $3 \times 10^{18}\text{ cm}^{-3}$ oxygen grown with the load-lock. The reason for the difference in definition for the two germanium fractions in the low oxygen case is because, even with the lock-lock, oxygen incorporates more readily into the 21% Ge layers than the 15% Ge films. To produce low oxygen 21% Ge layers requires growing a Si buffer layer for at least 16 minutes prior to $\text{Si}_{1-x}\text{Ge}_x$ film growth compared to only a 4 min Si buffer layer in the 14.5% Ge case. Using this buffer layer technique produced 21% Ge films with oxygen contents varying from less than the SIMS detection limit to about $3 \times 10^{18}\text{ cm}^{-3}$. The growth of Si itself plays an important role in reducing the background impurity concentration in the growth chamber.

Although the detailed mechanisms of oxygen incorporation are still unknown, these results indicate that the major source of oxygen in our LRP growth chamber is oxygen and/or water desorbing from the quartz walls. Having reduced this source via the addition of the load-lock chamber it should be possible to address other potential sources of oxygen such as the gasses themselves.

2. Thermal Stability Experiments

Experimental Approach

The general goal of these experiments was to quantify the effect of oxygen on misfit dislocation formation by comparing the annealing critical thicknesses of the high and low oxygen $\text{Si}_{1-x}\text{Ge}_x$ layers. We showed previously that the annealing critical thickness was defined as that strained layer thickness at a given Ge fraction below which misfit dislocations were not observed to form after an anneal of 850°C for 4 minutes. This severe annealing condition is a means of driving initially metastable films toward equilibrium. Such an experiment requires both high and low oxygen layers of various thicknesses. Hence, appropriate films were grown with Ge fractions of 14.5% and 21%. In each case the film thickness was varied from one to about five times the Matthew's equilibrium critical thickness (h_c =about 135\AA and 250\AA for 21% and 14.5% Ge alloys respectively). The resulting layers for the annealing experiments ranged from about 135\AA to 550\AA for the high and low oxygen 21% films and from 220\AA to 900\AA for the 14.5% layers and had few if any misfit dislocations in the as grown condition. Film thicknesses and compositions

were measured using RBS in a grazing angle geometry, with a scattering angle of 92°. Computer simulations were used to extract the film thickness and Ge fraction from the raw spectra.

The anneals were carried out in a lamp heated rapid thermal annealing (RTA) furnace using small pieces cleaved from the LRP wafers. Because of concerns about possible differences in the number of misfit dislocation nucleation sources between high and low oxygen films, large scratches were hand scribed into the $\text{Si}_{1-x}\text{Ge}_x$ layers in each sample to make nucleation equally easy in all cases. Prior to annealing the scribed samples were prepared using a modified RCA clean followed by a dip in a dilute solution of hydrofluoric acid (HF) and water. TEM specimens were prepared from the annealed samples using standard methods and examined using either the conventional TEMs available at Stanford or the HVTEM. In some cases x-ray topography was employed to confirm the results from the TEM experiments. The intent of these examinations was to determine whether or not misfit dislocations formed in the samples during the severe anneal and not to quantify the amount of dislocation formation by measuring average misfit dislocation spacings. In some cases it was necessary to examine more than one TEM specimen to reach the correct conclusion. For example in several specimens, misfit dislocations were not present far removed from the scratch but were evident in large numbers immediately adjacent (within 100 microns) to this region of crystalline damage. X-ray topography may also be misleading in the case of dislocations such as these close to the scratch.

It is important to note that oxide precipitates were not observed in any of these samples either prior to or after annealing. Most of the oxygen apparently remains in solution. Oxygen rich precipitates were observed, however, in some of our boron doped $\text{Si}_{1-x}\text{Ge}_x$ layers (not part of this experiment) after annealing for 60 hours at 900°C. These precipitates were often found at the intersection of orthogonal misfit dislocations at the hetero-interface. Heterogeneous nucleation was probably favorable in such areas. Clear signs of interactions between dislocations and precipitates were also observed. It is likely that one reason precipitates were not found in the layers used in the present experiments is due to a lack of nucleation sites.

The Annealing Critical Thickness

Figure 3 summarizes the TEM data from the annealing experiments for both the high and low oxygen $\text{Si}_{1-x}\text{Ge}_x$ layers. For the high oxygen films, no misfit dislocations were found in either 14.5% or 21% Ge layers as thick as two times the equilibrium critical thickness (Fig. 3 (a)). In contrast, misfit dislocations were found in the low oxygen layers at thicknesses very near the equilibrium values (Fig. 3 (b)). Care should be taken in interpreting this data because there are limits to the resolution of the TEM and x-ray topography for defining the yes/no dislocation transition. In addition, limitations exist in the RBS measurement of film thickness and Ge fraction. Such experimental errors when compounded make it difficult to conclude that the low oxygen layers exactly match the predictions of equilibrium theory. On the other hand, the large increase in thermal stability observed in the high oxygen films cannot be explained by these experimental uncertainties.

Misfit Dislocation Velocity

In situ heating experiments in the HVTEM were performed on the samples represented by the various data points in Fig.3 (a) and (b). Observations during *in situ* annealing were consistent with the results of the RTA furnace anneals/TEM examination experiments described above. Misfit dislocation formation was not observed in high oxygen films of thicknesses less than about two times the equilibrium critical thickness, whereas dislocation activity was evident in the low oxygen layers at thicknesses very near the equilibrium values. In addition, misfit dislocation velocity measurements were possible in many cases. Figure 4 shows the results of these measurements for the high and low oxygen layers:(a) 14.5% Ge films and (b) 21% Ge layers. The low oxygen films have consistently higher velocities than the high oxygen layers. We conclude therefore that the presence of oxygen substantially slows misfit dislocation propagation velocities in the LRP $\text{Si}_{1-x}\text{Ge}_x$ layers. This is strong evidence that the oxygen acts as a solid solution strengthening agent in the strained films. Solid solution strengthening and other possible explanations of how the oxygen interacts with the dislocations will be discussed briefly below. A more complete treatment of this subject will appear in Noble's dissertation and in the papers that will be published from his work.

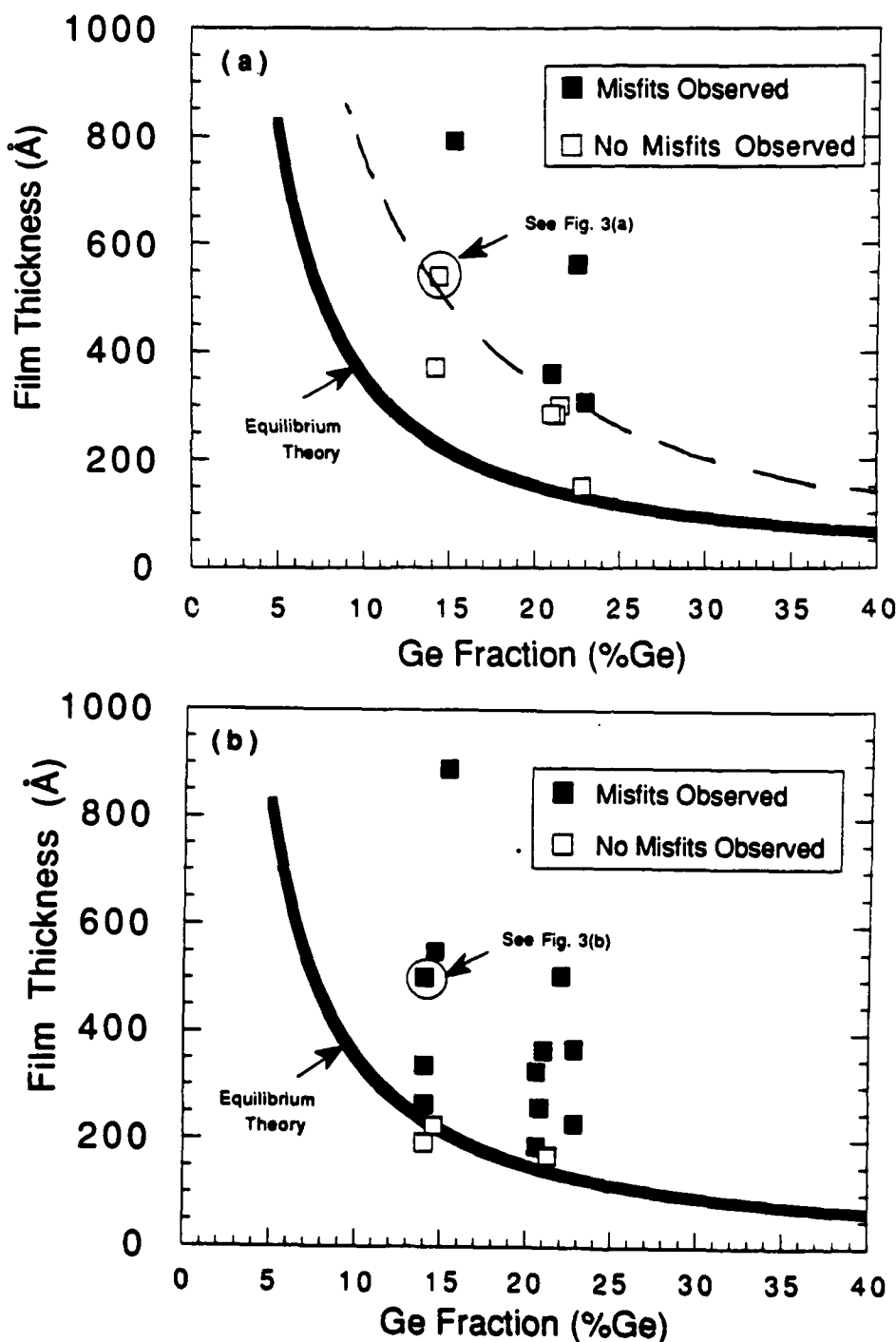


Figure 3 Thermal stability plots for (a) high oxygen films and (b) low oxygen layers. Shaded squares represent layers in which misfit dislocations were found after annealing at 850 °C for 4 minutes. Open squares signify films in which no misfit dislocations were found after the same anneal. The solid line represents the predictions of equilibrium theory. The high oxygen layers are about two times (dashed line) as stable as predicted by the theory, whereas the low oxygen layers match the theory very well.

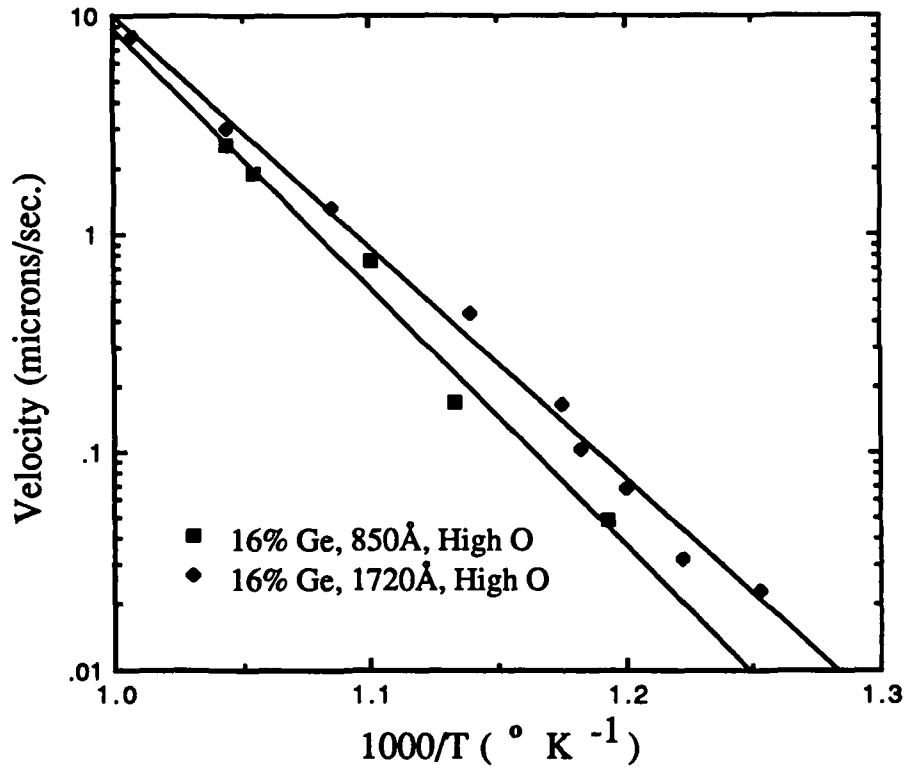


Figure 4 Misfit dislocation velocity measurements for (a) 14-16% Ge samples with both high and low oxygen contents. The presence of a high level of oxygen in the $\text{Si}_{1-x}\text{Ge}_x$ layers substantially slows misfit dislocation propagation.

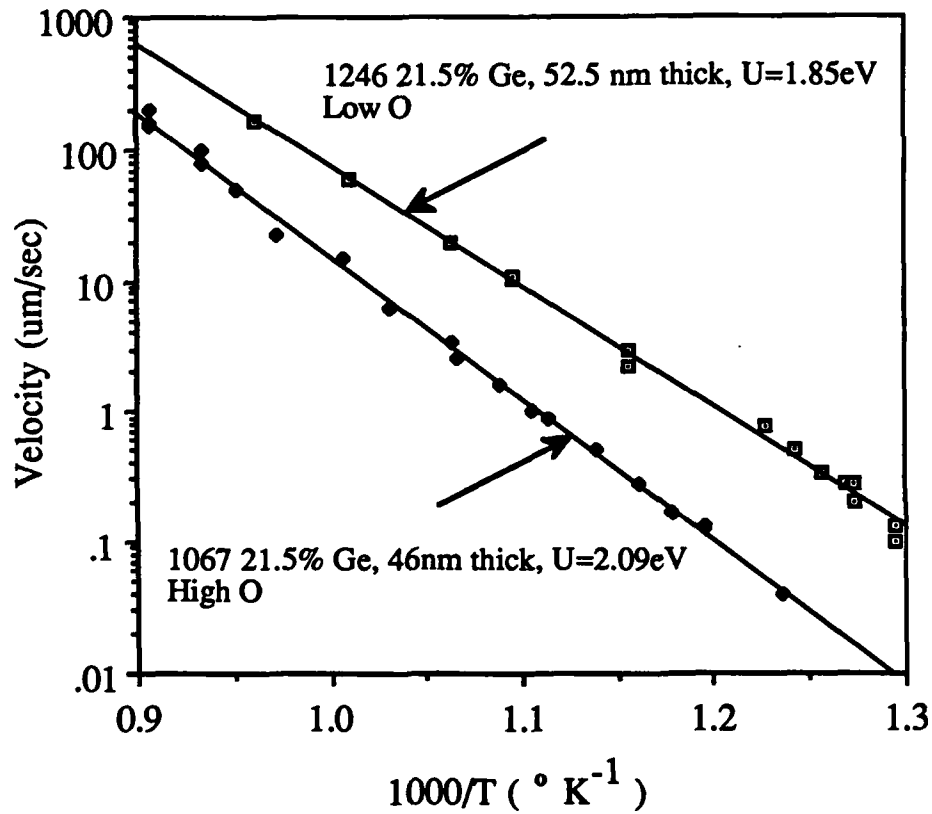


Figure 4 Misfit dislocation velocity measurements for (b) 21-22% Ge layers with both high and low oxygen. The presence of a high level of oxygen in the $Si_{1-x}Ge_x$ layers substantially slows misfit dislocation propagation.

3. Oxygen Strengthening Mechanisms

Before we consider possible explanations for how oxygen may strengthen the $\text{Si}_{1-x}\text{Ge}_x$ layers, we must first investigate the possibility that oxygen reduces the equilibrium lattice parameter of the films and thereby reduces the strain which is driving misfit dislocation formation. This idea is analogous to strain compensation by boron in $\text{Si}_{1-x}\text{Ge}_x$. X-ray double crystal rocking experiments were performed to measure the lattice parameter of the strained layers perpendicular to the hetero-interface for both the high and low oxygen films. This data can be converted to an equivalent Ge fraction in the layer using standard elastic constants. Germanium fractions measured in this way match those found using RBS to within 1 atomic percent Ge. We conclude that the oxygen does not substantially reduce the amount of strain in the high oxygen layers. Another way to think of this result is to ask the question: how much strain (Ge fraction) reduction would be necessary to explain the observed increase in thermal stability ascribed to the oxygen? Based on a 2x increase in film thickness required to cause misfit dislocation formation, the high oxygen 14.5% Ge films behave like equilibrium theory predicts 7% Ge layers should respond to severe annealing. In the same way 21% Ge high oxygen films act as though they were 12% Ge layers. The possible 1 percent Ge fraction difference measured by X-ray analysis and RBS is not nearly enough to explain the thermal stability enhancement.

Solid Solution Strengthening

The measured velocity difference between high and low oxygen containing $\text{Si}_{1-x}\text{Ge}_x$ layers is strong evidence that either dissolved oxygen or oxide micro-precipitates impede the motion of the misfit dislocation threading arm in the films with high oxygen content. Since micro-precipitates have not been observed, we will assume for the purpose of this analysis that all of the oxygen is uniformly distributed in solid solution. A simple solid solution strengthening model can then be used to predict a retarding stress due to the oxygen acting on the dislocation threading arm. This predicted retarding stress is in turn compared to the experimentally measured retarding stress in the high oxygen films. To make such a comparison possible the experimental data, which is in terms of an additional film thickness necessary to cause misfit dislocation formation, must be translated into an equivalent amount of stress by utilizing the concept of effective stress from our earlier work. We have found that the prediction of the model matches the experimental result quite well.

The formation of an oxygen atmosphere during RTA of $\text{Si}_{1-x}\text{Ge}_x$ films

Following the analysis of Cottrell, we can study the accumulation of oxygen atoms along the dislocation threading arm in the $\text{Si}_{1-x}\text{Ge}_x$ layers during the initial stages of the rapid thermal anneal given to the specimens to cause misfit dislocation formation. If we assume that the misfit dislocation threading arm is stationary, we can calculate the number of oxygen atoms which accumulate for a given thermal exposure. We have used standard methods to calculate $n(t)$, the number of oxygen atoms which have accumulated along a unit length of dislocation at a given time. Having calculated values of $n(t)$ we then need to determine whether the predicted amount of accumulated oxygen is enough to constitute a locking atmosphere. The simplest way of doing this is to realize that $1/n(t) = L$, where L is the average distance between oxygen atoms along the misfit dislocation threading arm. This obstacle spacing permits an estimate of the retarding stress due to the oxygen atmosphere for comparison to the experimentally measured retarding stress of 160 MPa. Following this method, predicted retarding stresses from oxygen solute atmospheres have been calculated. We note that L for a uniform distribution of 2×10^{20} oxygen atoms is about 60 Å. The predicted value of L from the present calculations is much greater than 60 Å except in the last 6 seconds of the heating ramp in a typical experiment. This indicates that a substantial atmosphere of oxygen forms only at temperatures of 600 °C and greater. Unfortunately, this is also the temperature range in which misfit dislocations start to move at substantial velocities. Therefore, from these calculations, we conclude that the competition between the formation of a locking oxygen atmosphere and dislocation propagation is close. It is not unreasonable to expect that the dislocation locking process could win out. Based on Sumino's results in elemental Si and the above analysis, it seems possible that dislocation locking by oxygen atmospheres could explain the enhanced thermal stability observed in the $\text{Si}_{1-x}\text{Ge}_x$ layers.

4. Nitrogen and Phosphorous Atmospheres

Sumino *et al.* have observed that in addition to oxygen, both nitrogen and phosphorous can strengthen elemental Si by the formation of locking Cottrell atmospheres. Based on this observation, we believe it may be possible to add nitrogen or phosphorous to $\text{Si}_{1-x}\text{Ge}_x$ films resulting in strained layers with enhanced thermal stability. At first glance, phosphorous would seem an ideal candidate since it is an n-type dopant for Si and Si_1-xGe_x . Unfortunately for many device applications a $\text{Si}_{1-x}\text{Ge}_x$ layer with heavy p-type doping is required. Another reason why phosphorous may not work in $\text{Si}_{1-x}\text{Ge}_x$ films is

because about an order of magnitude more phosphorous than oxygen is required to achieve the same amount of strengthening in elemental Si. If the same trend were followed in $\text{Si}_{1-x}\text{Ge}_x$ layers, about 10^{21} phosphorous ($\sim 7\%$) would be required for the same amount of strengthening due to 10^{20} oxygen atoms/cm³. Achieving such high doping levels is probably difficult if not impossible. On the other hand, only about 1/20th as much nitrogen as oxygen is required for comparable strengthening in Si. This suggests that only 5×10^{18} nitrogen atoms/cm³ may result in the same thermal stability enhancement as 10^{20} oxygen atoms/cm³ in $\text{Si}_{1-x}\text{Ge}_x$ layers.

5. Summary and Conclusions

The presence of 2×10^{20} oxygen atoms/cm³ in LRP-grown $\text{Si}_{1-x}\text{Ge}_x$ layers greatly enhances the thermal stability of these films. Since the oxygen does not substantially change the strained lattice constant of the layers, it is likely that the movement of the misfit dislocation threading arm is impeded by dissolved oxygen or oxygen micro-precipitates. Both solid solution strengthening by oxygen and dislocation pinning by Cottrell atmospheres of oxygen appear to be reasonable explanations of the experimental observations. More experimental information is required to distinguish between these two mechanisms. The addition of nitrogen or phosphorous as well as oxygen to $\text{Si}_{1-x}\text{Ge}_x$ layers may provide a method to impede misfit dislocation formation during high temperature annealing without reducing the strain and associated bandgap discontinuity in the films. The thermal budget for post-growth processing of these layers is increased due to the presence of oxygen. Two other methods for slowing the formation of misfit dislocations are presented in the next two chapters of this work.

6. References

1. K. Sumino, Defects and Properties of Semiconductors: Defect Engineering, edited by J. Chikawa, KTK Scientific Publishers, Tokyo, 227 (1987).
2. J.L. Hoyt, D.B. Noble, T. Ghani, C.A. King, J.F. Gibbons, M.P. Scott, S.S. Laderman, K. Nauka, J.E. Turner and T.I. Kamins, in International Conference on Electronic Materials 1990 Proceedings, Materials Research Society, Pittsburgh (in press)

III. ORAL PRESENTATIONS RESULTING FROM AFOSR GRANTS NO. 86-0051 AND 86-0051

1. W.D. Nix, "Mechanical Properties of Microelectronic Thin Film Materials", CIS Annual Review, Stanford University, March 6, 1986.
2. W.D. Nix, "New Experimental Techniques for the Study of Mechanical Properties of Microelectronic Thin Files", Department of Mechanical Engineering, University of California, Davis, March 13, 1986.
3. W.D. Nix, Mechanical Properties of Thin Films and Other Fine Scale Structures", Albuquerque Chapter of ASM, Albuquerque, New Mexico, March 19, 1986.
4. M.F. Doerner, "Mechanical Properties of Thin Films Using Nanoindenter Techniques", Materials Science Industrial Affiliates Program, Stanford University, May 28, 1986.
5. M.F. Doerner and W.D. Nix, "Mechanical Properties of Thin Films on Substrates", Micromechanics Research Group, IBM Research Laboratory, San Jose, California, June 27, 1986.
6. W.D. Nix and M.F. Doerner, "Mechanical Properties of Microelectronic Thin Film Materials: Nanoindenter and Wafer Curvature Techniques", Summer Research Group, Materials Science Center, Los Alamos National Laboratory, August 18, 1986.
7. W. D. Nix, "Mechanical Properties of Thin Films", Materials Science Colloquium, Department of Materials Science and Engineering, Stanford University, December 5, 1986.
8. W. D. Nix, "New Experimental Techniques for the Study of Mechanical Properties of Thin Films", Department of Metallurgical Engineering, The Ohio State University, Columbus, Ohio, February 6, 1987.
9. W.D. Nix, "Mechanical Properties of Thin Films", Department of Materials Science, Ecole Polytechnique de Federale Lausanne, Lausanne, Switzerland, April 15, 1987.
10. M.F. Doerner, "Mechanical Properties of Thin Films Using Sub-Micron Indentation Techniques", TMS Fall Meeting, Cincinnati, October 1987.
11. M.F. Doerner, "Stresses and Deformation Processes in Thin Films on Substrates", TMS Annual Meeting, Phoenix, Arizona, January 1988.
12. W.D. Nix, "Mechanical Properties of Thin Films", Intsitute of Metals Lecture, TMS Annual Meeting, Phoenix, Arizona, January 1988.
13. W.D. Nix, "Mechanical Properties of Thin Films and Other Finely Structured Materials", Micrometallurgy 88, TMS Northern California Meeting, Lake Tahoe, California, March 1988.

14. W.D. Nix, "Mechanisms and Kinetics of Misfit Dislocation Formation in Heteroepitaxial Structures", Symposium on Defects and Defect Reduction Processing in Semiconductor Heterostructures, Annual Meeting of the Metallurgical Society, Anaheim, California, February 19, 1990.
15. R. Venkatraman, J.C. Bravman, P.W. Davies, P.A. Flinn, D.B. Fraser and W.D. Nix, "Mechanical Properties and Microstructural Characterization of Al-0.5%Cu Thin Films", Symposium on Metallization for Electronics Applications, Annual Meeting of the Metallurgical Society, Anaheim, California, February 21, 1990.
16. A.I. Sauter and W.D. Nix, "Finite Element Calculations of Thermal Stresses in Passivated and Unpassivated Lines Bonded to Substrates", Symposium on Thin Films: Stresses and Mechanical Properties, Spring Meeting of the Materials Research Society, San Francisco, April 18, 1990.
17. W.D. Nix, D.B. Noble and J.F. Turlo, "Mechanisms and Kinetics of Misfit Dislocation Formation in Heteroepitaxial Structures", Symposium on Thin Films: Stresses and Mechanical Properties, Spring Meeting of the Materials Research Society, San Francisco, April 19, 1990.
18. W.D. Nix, "Mechanical Properties of Thin Films", Special Foreigner's Lecture, Japan Institute of Metals, Tohoku University, Japan, September 24, 1990.

IV. PUBLICATIONS RESULTING FROM AFOSR GRANTS NO. 89-0185 AND 86-0051

1. D.-B. Kao, J.P. McVittie, W.D. Nix and K.C. Saraswat, "Two-Dimensional Oxidation: Experiments and Theory", Proceedings of IEDM 85, IEEE, 1985, p. 388.
(selected as best student paper at the conference)
2. M.F. Doerner and W.D. Nix, "A Method for Interpreting the Data from Depth-Sensing Indentation Instruments", J. Materials Research, 1, 601 (1986).
3. M.F. Doerner, D.S. Gardner and W.D. Nix, "Plastic Properties of Thin Films on Substrates as Measured by Submicron Indentation Hardness and Substrate Curvature Techniques", J. Materials Research, 1, 845 (1986).
4. P.A. Flinn, D.S. Gardner and W.D. Nix, "Measurement and Interpretation of Stress in Aluminum-Based Metallization as a Function of Thermal History", IEEE Trans. on Electron Devices, ED-34, 689 (1987).
5. D.-B. Kao, J.P. McVittie, W.D. Nix and K.C. Saraswat, "Two-Dimensional Thermal Oxidation of Silicon - I. Experiments", IEEE Trans. on Electron Devices, ED-34, 1008 (1987).
6. D.-B. Kao, J.P. McVittie, W.D. Nix and K.C. Saraswat, "Two-Dimensional Thermal Oxidation of Silicon - II. Modelling Stress Effects in Wet Oxides", IEEE Trans. on Electron Devices, ED-35, 25 (1988).

7. M.L. Ovecoglu, M.F. Doerner and W.D. Nix, "Elastic Interactions of Screw Dislocations in Thin Films on Substrates", Acta Metall., 35, 2947 (1987).
8. M.F. Doerner and W.D. Nix, "Stresses and Deformation Processes in Thin Films on Substrates", CRC Critical Reviews of Solid State and Materials Sciences, 14, 225 (1988).
9. M.F. Doerner and S. Brennan, "Strain Distribution in Thin Aluminum Films using X-Ray Depth Profiling", J. Appl. Phys., 63, 126 (1988).
10. J.C. Bravman, W.D. Nix, D.M. Barnett and D.A. Smith (Editors), "Thin Films: Stresses and Mechanical Properties", Materials research Symposium Proceedings, 130. (1989).
11. F.J. von Preissig, "Applicability of the Classical Curvature-Stress Relation for Thin Films on Plate Substrates", J. Appl. Phys., 66, 4262 (1989).
12. W.D. Nix, "Mechanical Properties of Thin Films", Metall. Trans. A, 20A, 2217 (1989).
13. A.I. Sauter and W.D. Nix, "Finite Element Calculations of Thermal Stresses in Passivated and Unpassivated Lines Bonded to Substrates", Materials Research Symposium Proceedings, 188, 15-20 (1990).
14. W.D. Nix, D.B. Noble and J.F. Turlo, "Mechanisms and Kinetics of Misfit Dislocation Formation in Heteroepitaxial Thin Films", Materials Research Symposium Proceedings, 188, 315-330 (1990).
15. E.Arzt and W.D. Nix, "A Model for the Effect of Line Width and Mechanical Strength on Electromigration Failure of Interconnects with "Near-Bamboo" Grain Structures", (accepted for publication in Journal of Materials Research)
16. W.D. Nix and E. Arzt, "On Void Nucleation and Growth in Metal Interconnect Lines under Electromigration Conditions", (accepted for publication in Metall. Trans.)